

COHERENT CURVATURE RADIATION BY BUNCHES IN THREE-DIMENSIONAL MAGNETIC FIELD GEOMETRY: APPLICATION TO PULSARS AND FAST RADIO BURSTS

YUAN-PEI YANG^{1,2} AND BING ZHANG^{1,3,4}¹Kavli Institute for Astronomy and Astrophysics, Peking University, Beijing 100871, China; yypspore@gmail.com;²KIAA-CAS Fellow³Department of Astronomy, School of Physics, Peking University, Beijing 100871, China⁴Department of Physics and Astronomy, University of Nevada, Las Vegas, NV 89154, USA; zhang@physics.unlv.edu

Draft version June 22, 2019

ABSTRACT

The extremely high brightness temperatures of pulsars and fast radio bursts (FRBs) require their radiation mechanisms to be coherent. Curvature radiation by bunches is often discussed as a favored mechanism. We develop a general radiation theory of coherent curvature radiation by bunches under three-dimensional magnetic field geometry from the first principles. We consider a bunch characterized by the bunch length, curvature radius of the trajectory family, bunch opening angle, and electron energy distribution. We find that the spectrum of coherent curvature radiation is a multi-segment broken power law, with the break frequencies depending on bunch properties and trajectory configuration. Different from previous works, we find that in the pulsar magnetosphere only fluctuating *net* charges with respect to the Goldreich-Julian outflow can make a contribution to coherent radiation. We apply this model to constrain the observed spectra of pulsars and FRBs. For a typical pulsar ($B_p = 10^{12}$ G and $P = 0.1$ s), a small fluctuation of net charge: e.g., $\delta n_{\text{GJ}} \sim 0.1 n_{\text{GJ}}$, can provide the observable flux. For FRBs, the fluctuating net charge may be larger due to its abrupt nature. For $\delta n_{\text{GJ}} \sim n_{\text{GJ}}$, a neutron star with strong magnetic field and fast rotation is required to power an FRB in the spindown-powered model. The requirement is less stringent for the cosmic comb model thanks to the larger cross section and compressed charge density of the bunch made by the external astrophysical stream that combs the magnetosphere.

Subject headings: radiation mechanisms: non-thermal — radio continuum: general

1. INTRODUCTION

Both radio pulsars and fast radio bursts (FRBs) show non-thermal radio spectra and a very high brightness temperature, T_B , which is much greater than any plausible thermal temperature, T_e , of the electrons in the source. In general, there are two mechanisms that limit the brightness temperature in a synchrotron source (e.g. Melrose 2017): 1. synchrotron self-absorption (SSA) implies $T_B \lesssim \gamma m_e c^2 / k_B$, where γ is the Lorentz factor of the electrons; 2. inverse Compton scattering implies $T_B \lesssim 10^{12}$ K (Kellermann & Pauliny-Toth 1969). Observationally, the brightness temperature of radio pulsars can reach $T_B \sim 10^{26}$ K, and the brightness temperature of FRBs can even reach $T_B \sim 10^{37}$ K. Therefore, the emission mechanism from pulsars and FRBs must be coherent¹, which means that the observed emission cannot be explained by the simple summation of the radiation power of individual particles, so that the superposition of the electromagnetic waves from each particle should be considered. Theoretical models usually invoke one of three classes of coherent emission mechanisms (e.g. Melrose 2017): radiation by bunches (related to particle coherence in position space), a reactive instability (related to particle coherence in momentum space), and a

maser mechanism (negative absorption).

The coherent emission mechanism of radio pulsars remains poorly understood. Suggested mechanisms include coherent curvature radiation by bunches (Gunn & Ostriker 1971; Sturrock 1971; Ginzburg & Zhelezniakov 1975; Ruderman & Sutherland 1975; Buschauer & Benford 1976; Benford & Buschauer 1977; Gil et al. 2004), various maser mechanisms (Twiss 1958; McCray 1966; Blandford 1975; Melrose 1978; Luo & Melrose 1992, 1995), linear acceleration emission (Cocke 1973; Melrose 1978; Kroll & McMullin 1979), relativistic plasma emission (Weatherall 1998; Melrose & Gedalin 1999; Melrose 2017), and anomalous Doppler emission (Machabeli & Usov 1979; Kazbegi et al. 1991; Lyutikov et al. 1999a,b). From the theoretical point of view, none of these emission mechanisms is obviously favorable than the others so far (Melrose 2017). For FRBs, their progenitors and radiation mechanism are still mysterious. Their extremely high brightness temperature would need more stringent coherent conditions than that of pulsars (e.g. Lorimer et al. 2007; Thornton et al. 2013; Chatterjee et al. 2017). Up to now, most FRB models invoke coherent curvature radiation by bunches to explain the FRB emission. However, the coherent condition is over-simplified in most FRB models, which only assumes that the bunch length is much smaller than the wavelength of GHz wave. Besides curvature radiation by bunches (Katz 2014; Kumar et al. 2017; Ghisellini & Locatelli 2017;

¹ In physics, two waves with the same waveform are perfectly coherent if they have a constant phase difference and the same frequency. Thus, coherence can cause the amplitude of the superposition of two wave enhanced or reduced. In the field of pulsars and FRBs, “coherent” is mainly defined as “coherently enhanced”. We adopt this definition throughout the paper.

(Lu & Kumar 2017), some maser mechanisms (Ghisellini 2017; Lyubarsky 2014; Waxman 2017; Beloborodov 2017) have also been proposed to explain FRB emission. However, the maser condition of population inversion is hard to achieve, especially for the extremely high brightness temperature observed in FRBs (Lu & Kumar 2017).

In this paper, we mainly focus on the coherent curvature radiation by bunches. When a charged particle moves along a curved trajectory, its perpendicular acceleration will result in the so called “curvature radiation”. For a relativistic electron in the magnetosphere around a neutron star, due to the strong magnetic field, the vertical momentum perpendicular to the field line quickly drops to zero in a very short period of time due to synchrotron cooling, e.g., $t_{\text{cool}} \sim 10^{-18} \text{ s}(\gamma/1000)(B/10^{12} \text{ G})$, where γ is the Lorentz factor of electron and B is the magnetic field strength. This leads to the electron moving along with the field line. The trajectory then essentially overlap with the field line².

In the following, we attempt to develop a general radiation theory of the curvature radiation by bunches under a three-dimensional magnetic field geometry from the first principles, and apply this model to pulsars and FRBs. We consider that a bunch, consisting of a trajectory family, is characterized by the following parameters: bunch length, curvature radius of the trajectory family, bunch opening angle, and electron energy distribution. We find that the radiation spectra of bunches under a three-dimensional magnetic field geometry is a multi-segment broken power law with the break frequencies depending on the above parameters. Consider that the observed duration of one pulse from pulsars or FRBs, e.g., $T_{\text{obs}} \gtrsim 1 \text{ ms}$ is much longer than the pulse duration of the curvature radiation, e.g. $T_p \sim 1/\nu_{\text{obs}} \sim 1 \text{ ns}$, there will be more than one bunch sweeping cross the line of sight during the observed duration. In fact, we note that not all electrons in the magnetosphere contributes to coherent radiation, and only the fluctuating net charges with respect to the Goldreich-Julian outflow can make a contribution, which might originate from the abrupt discharges of the inner gap near the neutron star surface (Ruderman & Sutherland 1975; Zhang et al. 1997; Gil & Sendyk 2000), instabilities in the outflow (Egorenkov et al. 1983; Gedalin et al. 2002; Kumar et al. 2017; Lu & Kumar 2017), or the oscillation of plasma in the acceleration region (Levinson et al. 2005; Beloborodov & Thompson 2007; Luo & Melrose 2008). For all these cases, the fluctuating net charge in one bunch usually cannot be much larger than the local Goldreich-Julian density for pulsars. Finally, we use our model to constrain the observations of pulsars and FRBs.

The paper is organized as follows. In Section 2, we briefly review the properties of the radiation from a single moving charge. In Section 3, we calculate the coherent curvature radiation from a point source. In Section 4, we discuss the coherent curvature radiation from an extended source, including electrons in the same trajec-

tory and electrons in a trajectory family. In Section 5, the curvature radiation from a three-dimensional bunch is obtained. In Section 6 and Section 7, we discuss the applications to pulsars and FRBs, respectively. The results are summarized in Section 8 with some discussion. Some detailed calculations are presented in the Appendix.

2. RADIATION BY MOVING CHARGES

First, we briefly summarize the electromagnetic field from a single moving charge. The fields at a point \mathbf{x} at time t is determined by the retarded position $\mathbf{r}(t_{\text{ret}})$ and time t_{ret} of the charged particle. We define $\mathbf{R} \equiv \mathbf{x} - \mathbf{r}(t_{\text{ret}})$, $\mathbf{n} \equiv \mathbf{R}/R$ and $\boldsymbol{\beta} \equiv \dot{\mathbf{r}}(t_{\text{ret}})/c$, then the electromagnetic fields are given by (e.g. Jackson 1998; Rybicki & Lightman 1979)

$$\begin{aligned} \mathbf{B}(\mathbf{x}, t) &= [\mathbf{n} \times \mathbf{E}(\mathbf{x}, t)]_{\text{ret}} \\ \mathbf{E}(\mathbf{x}, t) &= e \left[\frac{\mathbf{n} - \boldsymbol{\beta}}{\gamma^2(1 - \mathbf{n} \cdot \boldsymbol{\beta})^3 R^2} \right]_{\text{ret}} \\ &\quad + \frac{e}{c} \left[\frac{\mathbf{n} \times \{(\mathbf{n} - \boldsymbol{\beta}) \times \dot{\boldsymbol{\beta}}\}}{(1 - \mathbf{n} \cdot \boldsymbol{\beta})^3 R} \right]_{\text{ret}}, \end{aligned} \quad (1)$$

where the subscript “ret” means that the quantities in the square brackets are all to be evaluated at the retarded time t_{ret} . As shown in the above equations, the electric field is composed of two terms: (1) the velocity field (e.g. Rybicki & Lightman 1979): it is the generalization of the Coulomb law to a moving charge, and falls off as $1/R^2$; (2) the acceleration field: along with the corresponding magnetic field, it constitutes the radiation field, and falls off as $1/R$.

Based on the above time-dependent fields, e.g., $\mathbf{E}(\mathbf{x}, t)$ or $\mathbf{B}(\mathbf{x}, t)$, the frequency spectrum can be calculated by the Fourier transformation. According to Appendix A, the energy radiated per unit solid angle per unit frequency interval is given by (e.g. Jackson 1998; Rybicki & Lightman 1979)

$$\frac{dI}{d\omega d\Omega} = \frac{e^2 \omega^2}{4\pi^2 c} \left| \int_{-\infty}^{+\infty} \mathbf{n} \times (\mathbf{n} \times \boldsymbol{\beta}) e^{i\omega(t - \mathbf{n} \cdot \mathbf{r}(t)/c)} dt \right|^2. \quad (2)$$

Note that the time in the above integral corresponds to the retarded time of the moving charge, rather than the observed time at the field point. If there is more than one charge that is accelerated, a coherent sum of the amplitudes should replace the single amplitude in the above equation. In this case, the energy radiated per unit solid angle per unit frequency interval is given by

$$\frac{dI}{d\omega d\Omega} = \frac{\omega^2}{4\pi^2 c} \left| \int_{-\infty}^{+\infty} \sum_j q_j \mathbf{n} \times (\mathbf{n} \times \boldsymbol{\beta}_j) e^{i\omega(t - \mathbf{n} \cdot \mathbf{r}_j(t)/c)} dt \right|^2, \quad (3)$$

where j represents the identifier of each charged particle, and q_j is the corresponding charge.

We should note that $dI/d\omega d\Omega$ does not have “per unit time” in its dimension. As pointed out by Rybicki & Lightman (1979), the coexist of dt and $d\omega$ would violate the uncertainty relation between ω and t ,

² In fact, the curved trajectory does not strictly overlap with the field line. There is a small drift velocity due to the Lorentz force (e.g. Zhelezniakov & Shaposhnikov 1979).

e.g., $\Delta t \Delta \omega > 1$. However, if the pulse repeats on an average time scale T , the radiation power may be written as (Rybicki & Lightman 1979)

$$\frac{dW}{d\omega d\Omega dt} \equiv \frac{1}{T} \frac{dI}{d\omega d\Omega}. \quad (4)$$

Therefore, for the synchrotron radiation, naturally the pulse repeats with the gyration period $T = 2\pi/\omega_B$, where $\omega_B = eB/\gamma m_e c$ is the gyration frequency. However, for curvature radiation of a single particle, the charge motion direction only sweeps the line of sight one time, so that the definition of the radiation power is no longer meaningful. If there are more than one particles sweeping cross the line of sight, T would be the mean time interval between each pair of the particles, and $dI/d\omega d\Omega$ corresponds to the radiation energy of one particle³.

3. COHERENT EMISSION BY CHARGES IN A POINT SOURCE

In this section, we calculate the radiation from a point source, containing one or more electrons and moving instantaneously at a constant speed on an approximate circular path. In order to satisfy the point-source approximation, one needs: 1. the system scale is much less than the typical curvature radius of the trajectory; 2. all electrons have nearly the same state of initial motion⁴. In this section, we consider three cases for the point-source radiation: 1. a single electron; 2. power-law-distributed electrons; 3. particles with different charges.

3.1. Radiation from a single electron

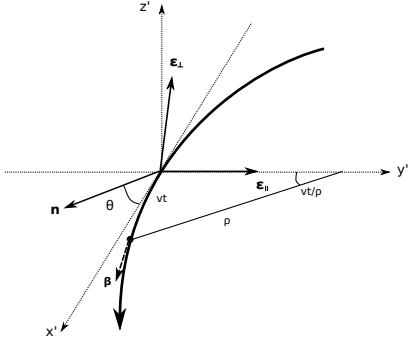


FIG. 1.— Geometry for an instantaneously circular motion. The trajectory lies in the $x' - y'$ plane. At the retarded time $t = 0$, the electron is at the origin, and the velocity is along the x' axis.

Before discussing more complex scenarios, we briefly summarize the curvature radiation of a single electron during instantaneously circular motion (e.g. Jackson 1998). For an accelerated relativistic electron, the radiation is beamed in a narrow cone in the direction of the electron's velocity, which can be seen as a short pulse as the beam sweeps cross the observational point. Consider

³ Here we have assumed that the emission pulse is incoherent. If the superposition from the electromagnetic wave from each source is coherent, T would be the mean time interval of each coherent pulse, and $dI/d\omega d\Omega$ corresponds to the radiation energy of one coherent pulse.

⁴ For relativistic electrons with different energies, although the energy difference could be large, their velocities are close to the speed of light.

the appropriate coordinate system in Figure 1, where the origin is the location of the electron at the retarded time $t = 0$, and the instantaneously-circular trajectory lies in the $x' - y'$ plane with a curvature radius ρ . The electron velocity is along x' axis at $t = 0$. Since the integral in Eq.(2) is taken over the trajectory, \mathbf{n} can be chosen to lie in the $x' - z'$ plane without losing generality. ϵ_{\parallel} is the unit vector pointing to the center of the instantaneous circle, which is set to the y' direction, and $\epsilon_{\perp} = \mathbf{n} \times \epsilon_{\parallel}$ is defined. The energy radiated per unit frequency interval per unit solid angle is given by (e.g. Jackson 1998)

$$\begin{aligned} \frac{dI}{d\omega d\Omega} &= \frac{e^2 \omega^2}{4\pi^2 c} |-\epsilon_{\parallel} A_{\parallel} + \epsilon_{\perp} A_{\perp}|^2 = \frac{e^2}{3\pi^2 c} \left(\frac{\omega \rho}{c}\right)^2 \\ &\times \left(\frac{1}{\gamma^2} + \theta^2\right)^2 \left[K_{2/3}^2(\xi) + \frac{\theta^2}{(1/\gamma^2) + \theta^2} K_{1/3}^2(\xi)\right], \end{aligned} \quad (5)$$

where A_{\perp} and A_{\parallel} are the polarized components of the amplitude along ϵ_{\perp} and ϵ_{\parallel} , respectively, which are given by

$$\begin{aligned} A_{\parallel} &= \frac{2i}{\sqrt{3}} \frac{\rho}{c} \left(\frac{1}{\gamma^2} + \theta^2\right) K_{2/3}(\xi), \\ A_{\perp} &= \frac{2}{\sqrt{3}} \frac{\rho \theta}{c} \left(\frac{1}{\gamma^2} + \theta^2\right)^{1/2} K_{1/3}(\xi). \end{aligned} \quad (6)$$

The argument ξ in the modified Bessel function is defined as

$$\xi = \frac{\omega \rho}{3c} \left(\frac{1}{\gamma^2} + \theta^2\right)^{3/2}. \quad (7)$$

According to the properties of the modified Bessel function, e.g., $K_{\nu}(\xi) \rightarrow 0$ for $\xi \gg 1$, the radiation intensity is negligible for $\xi \gg 1$. As shown in Eq.(7), $\xi \gg 1$ is satisfied at large angles. On the other hand, if ω becomes too large, ξ will be large at all angles. Therefore, one can define the critical frequency by $\xi = 1/2$ for $\theta = 0$, beyond which the radiation can be negligible at all angles (e.g. Jackson 1998). Such a critical frequency is given by

$$\omega_c = \frac{3}{2} \gamma^3 \left(\frac{c}{\rho}\right). \quad (8)$$

For an accelerated relativistic electron, its radiation is beamed in a narrow cone that sweeps cross the line of sight, which means that the radiation concentrates around $\theta = 0$, and the parallel polarized component is dominant. According to Eq.(5) and the properties of the modified Bessel function, e.g., $K_{\nu}(x) \rightarrow (\Gamma(\nu)/2)(x/2)^{-\nu}$ for $x \ll 1$ and $\nu \neq 0$, and $K_{\nu}(x) \rightarrow \sqrt{\pi/2x} \exp(-x)$ for $x \gg 1$ and $\nu \neq 0$, one has (e.g. Jackson 1998)

$$\left. \frac{dI}{d\omega d\Omega} \right|_{\theta=0} \simeq \begin{cases} \frac{e^2}{c} \left[\frac{\Gamma(2/3)}{\pi}\right]^2 \left(\frac{3}{4}\right)^{1/3} \left(\frac{\omega \rho}{c}\right)^{2/3} & \omega \ll \omega_c \\ \frac{3}{4\pi} \frac{e^2}{c} \gamma^2 \frac{\omega}{\omega_c} e^{-\omega/\omega_c} & \omega \gg \omega_c \end{cases}. \quad (9)$$

For simplicity, we use the following approximation:

$$\frac{dI}{d\omega d\Omega} \simeq \frac{e^2}{c} \left[\frac{\Gamma(2/3)}{\pi}\right]^2 \left(\frac{3}{4}\right)^{1/3} \left(\frac{\omega \rho}{c}\right)^{2/3} e^{-\omega/\omega_c} \quad (10)$$

where the subscript $\theta = 0$ has been omitted for brevity. For a given frequency ω , the spread in angle can be estimated by determining the angle θ_c at which $\xi(\theta_c) = \max(\xi(0), 1)$. One has (Jackson 1998)

$$\theta_c(\omega) \simeq \begin{cases} \frac{1}{\gamma} \left(\frac{2\omega_c}{\omega} \right)^{1/3} = \left(\frac{3c}{\omega\rho} \right)^{1/3} & \omega \ll \omega_c \\ \frac{1}{\gamma} \left(\frac{2\omega_c}{3\omega} \right)^{1/2} & \omega \gg \omega_c \end{cases}. \quad (11)$$

As shown in the above equation, for frequencies comparable to ω_c , the radiation is confined to angles of the order $\sim 1/\gamma$; for smaller frequencies, the angular spread is larger. Note that for frequencies larger than ω_c , one has $\theta_c \propto \omega^{-1/2}$. However, the radiation has become negligible due to the exponential term, see Eq.(9) or Eq.(10).

The spectrum of the total energy emitted as the electron passes can be found by integrating Eq.(5) over angles

$$\frac{dI}{d\omega} = \sqrt{3} \frac{e^2}{c} \gamma \frac{\omega}{\omega_c} \int_{\omega/\omega_c}^{\infty} K_{5/3}(x) dx. \quad (12)$$

The above equation can give the classical spectrum of synchrotron radiation in astrophysical processes. However, one must note that it is the total radiation spectrum in all directions rather than the direction along the line of sight. In most astrophysical sources that invoke synchrotron radiation, since electrons in the magnetic fields have random pitch angles (the angle between the magnetic field direction and the electron velocity direction), or the local magnetic fields where electrons are accelerated have random directions, the incoherent sum of the radiation energy per unit solid angle, e.g., Eq.(5), from different electrons will make the classical $\omega^{1/3}$ spectrum as shown in Eq.(12). However, for curvature radiation, Eq.(12) is not applicable for the following two reasons: 1. the trajectories of charged sources are almost the same at large scales, and the observed spectrum is from the radiation along the line of sight; 2. even for more than one charged sources with different motion directions, a coherent sum of the amplitudes, rather than a simple integration of radiation energy over angles, should be considered.

Finally, we consider the duration of one pulse emitted by such an instantaneously circular motion. For a given frequency with $\omega \ll \omega_c$, the spread in angle is $\theta_c(\omega) \simeq (3c/\omega\rho)^{1/3}$. Thus, the frequency-dependent pulse duration of the curvature radiation is given by

$$T_p(\omega) = \frac{\rho\theta_c(\omega)}{c} \left(1 - \frac{v}{c}\right) \simeq \frac{1}{2\gamma^2} \left(\frac{3\rho^2}{c^2\omega}\right)^{1/3}, \quad (13)$$

where the factor $(1 - v/c)$ is due to the time-delay effect. For $\omega \sim \omega_c$, one has $T_p \sim \rho/c\gamma^3 \sim 1/\omega_c$.

3.2. Radiation from electrons with power-law distribution

Next, we assume the energy distribution of the electrons satisfies a power-law distribution, e.g.

$$N_e(\gamma)d\gamma = N_{e,0} \left(\frac{\gamma}{\gamma_1}\right)^{-p} d\gamma, \quad \gamma_1 < \gamma < \gamma_2 \quad (14)$$

where $N_e(\gamma)d\gamma$ is the electron number in a range from γ to $\gamma + d\gamma$, $N_{e,0}$ is the corresponding normalization, and γ_1 and γ_2 are the lower and upper limits of the Lorentz factor. In this case, a coherent sum of the amplitudes should replace the single amplitude in Eq.(5), i.e.

$$\frac{dI}{d\omega d\Omega} = \frac{e^2\omega^2}{4\pi^2 c} \left| -\epsilon_{\parallel} \int_{\gamma_1}^{\gamma_2} N_e(\gamma) A_{\parallel}(\omega, \gamma) d\gamma + \epsilon_{\perp} \int_{\gamma_1}^{\gamma_2} N_e(\gamma) A_{\perp}(\omega, \gamma) d\gamma \right|^2. \quad (15)$$

Since the radiation concentrates around $\theta = 0$ for curvature radiation, we assume that the observed direction is at $\theta = 0$, which means that $A_{\perp}(\omega, \gamma) = 0$. According to Appendix B, for a power-law electron distribution, the energy radiated per unit frequency interval per unit solid angle is given by

$$\frac{dI}{d\omega d\Omega} \simeq \frac{e^2}{c} \frac{2^{(2p-6)/3}}{3\pi^2} \left[\Gamma\left(\frac{2}{3}\right) \Gamma\left(\frac{p-1}{3}\right) \right]^2 N_{e,0}^2 \gamma_1^4 \times \begin{cases} \left(\frac{\omega}{\omega_{c1}}\right)^{2/3} & \omega \ll \omega_{c1} \\ \left(\frac{\omega}{\omega_{c1}}\right)^{-(2p-4)/3} e^{-\omega/\omega_{c2}} & \omega \gg \omega_{c1} \end{cases}, \quad (16)$$

where $\omega_{c1} = \omega_c(\gamma_1)$ and $\omega_{c2} = \omega_c(\gamma_2)$. At last, we note that the velocity spread, e.g., $\Delta v \sim \Delta\beta c \sim \Delta\gamma c/\gamma^3$, would cause a linear extent of the bunch, i.e., $\Delta l \sim \Delta v t \sim ct/\gamma^2$, where $\Delta\gamma \sim \gamma$ is assumed. For the electromagnetic wave with $\lambda \gtrsim \Delta l$, the effect of the linear extent is negligible.

3.3. Radiation from the particles with different charges

Next, we discuss the radiation from a point source with different charged particles. According to Eq.(3), if all the charged particles have the same trajectory, the charge term can be extracted from the integral, e.g.,

$$\frac{dI}{d\omega d\Omega} = \frac{\omega^2}{4\pi^2 c} \left(\sum_j^N q_j \right)^2 \times \left| \int_{-\infty}^{+\infty} \mathbf{n} \times (\mathbf{n} \times \boldsymbol{\beta}) e^{i\omega(t - \mathbf{n} \cdot \mathbf{r}(t)/c)} dt \right|^2. \quad (17)$$

Therefore, only the net charge in the point source can contribute to the curvature radiation. For example, in the pulsar wind, the total electron number density is often taken as $\mu_{\pm} n_{\text{GJ}}$, where n_{GJ} denotes the Goldreich-Julian density (Goldreich & Julian 1969), and μ_{\pm} is the multiplicity resulting from the electron-positron pair cascade. However, the electron-positron pairs in a bunch do not contribute to the net charge, and hence, would not contribute to coherent emission. Only the net charge, of the order of n_{GJ} , in the bunch contributes to the coherent radiation.

4. COHERENT EMISSION BY CHARGES IN AN EXTENDED SOURCE

In the above section, the size of the emission region is assumed to be much smaller than the curvature radius of the trajectory, which can be treated as a point

source. Next, we further consider the curvature radiation from an extended source, including three cases: 1. the electrons move in the same trajectory but with different delay times; 2. the electrons are in a trajectory family with the same curvature radius but different orientations; 3. the electrons are in the trajectories with different curvature radii.

4.1. Electrons in the same trajectory

If the trajectories of N electrons are the same but with electrons injected at different times, the retarded position of the j th electron can be written as $\mathbf{r}_j(t) = \mathbf{r}(t + \Delta t_j) \simeq \mathbf{r}(t) + \boldsymbol{\beta}(t)c\Delta t_j$, where Δt_j is the retarded delay time between the first electron and the j th electron. Furthermore, if the velocity does not change significantly during Δt_N , $\boldsymbol{\beta}$ would be independent of the time during Δt_N , leading to $\boldsymbol{\beta}(t) \simeq \boldsymbol{\beta}$ and $\beta_j \simeq \beta$. In this case, the retarded position of the j th electron would be $\mathbf{r}_j(t) \simeq \mathbf{r}(t) + \Delta \mathbf{r}_j$, where $\Delta \mathbf{r}_j \simeq \boldsymbol{\beta}c\Delta t_j$ is the relative retarded displacement between the j th electron and the first electron. According to Eq.(3), the total energy radiated per unit solid angle per unit frequency interval can be approximately given by

$$\frac{dI_{(N)}}{d\omega d\Omega} \simeq \frac{e^2\omega^2}{4\pi^2c} \left| \int_{-\infty}^{+\infty} \mathbf{n} \times (\mathbf{n} \times \boldsymbol{\beta}) e^{i\omega(t - \mathbf{n} \cdot \mathbf{r}(t)/c)} dt \right|^2 \times \left| \sum_j^N e^{-i\omega(\mathbf{n} \cdot \Delta \mathbf{r}_j/c)} \right|^2, \quad (18)$$

which is

$$\frac{dI_{(N)}}{d\omega d\Omega} = \frac{dI_{(1)}}{d\omega d\Omega} F_\omega(N), \quad (19)$$

where

$$F_\omega(N) = \left| \sum_j^N e^{-i\omega(\mathbf{n} \cdot \Delta \mathbf{r}_j/c)} \right|^2, \quad (20)$$

and $dI_{(1)}/d\omega d\Omega$ corresponds to the radiation of the first electron. Therefore, once $F_\omega(N)$ is obtained, the radiation spectrum of N electrons can be calculated via Eq.(19) and Eq.(20). For example, if all the electrons are at one point, e.g., $\Delta \mathbf{r}_j \simeq 0$, one has $F_\omega(N) = N^2$, which means that the spectrum has the same shape with the single charge, but is enhanced by a factor of N^2 .

4.1.1. One bunch in the trajectory

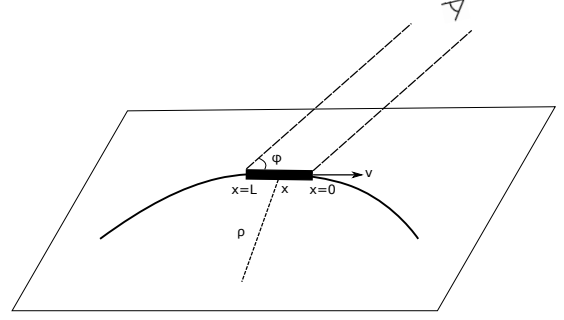


FIG. 2.— Curvature radiation from a bunch. The dark strip denotes the bunch with length L and N electrons, and the curve denotes the bunch trajectory.

We assume that electrons are normally distributed in a bunch that is along the trajectory. As shown in Figure 2, in the lab frame, the intrinsic length of a bunch is L , the curvature radius of the trajectory is ρ , the angle between the bunch velocity and the line of sight is φ , and the position of the j electron is x_j ($0 < x_j < L$). Then the amplitude of the radiation from the j th electron is given by

$$\mathbf{A}(\omega, x_j) = \mathbf{A}(\omega, 0) e^{-ikx_j \cos \varphi}, \quad (21)$$

where $k \equiv \omega/c$, \mathbf{A} is the radiation amplitude (see Appendix A), and $\mathbf{A}(\omega, 0)$ corresponds to the radiation amplitude of the first electron. According to Eq.(20), one has

$$F_\omega(N) = \left| \sum_j^N e^{-ikx_j \cos \varphi} \right|^2 = \left| \frac{N}{L} \int_0^L e^{-ikx \cos \varphi} dx \right|^2 = N^2 \left| \frac{1 - e^{-ikL \cos \varphi}}{ikL \cos \varphi} \right|^2 = N^2 \left[\frac{\sin(\omega/\omega_l)}{(\omega/\omega_l)} \right]^2 \quad (22)$$

where

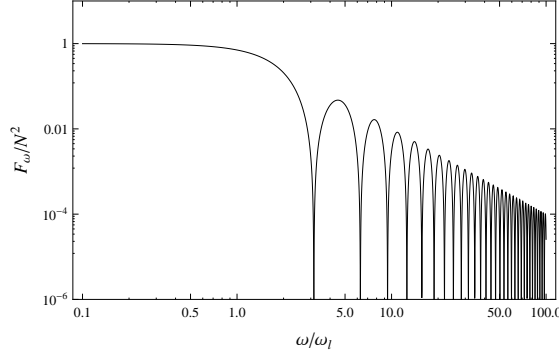
$$\omega_l = \frac{2c}{L \cos \varphi}. \quad (23)$$

For the relativistic electron, the radiation is beamed along the velocity direction and sweeps cross the line of sight. Therefore, the radiation can be significantly observed only when $\varphi \sim 1/\gamma^2$, and one has $\omega_l \simeq 2c/L$. As shown in Eq.(22), $F_m(N) \sim N^2$ for $\omega \ll \omega_l$, and $F_m(N) \propto \omega^{-2}$ for $\omega \gg \omega_l$. However, we should note that there is a maximum ω beyond which Eq.(22) is not applicable. The reason is the following: the emission angle of the relativistic electron is $\theta_c \sim (3c/\omega\rho)^{1/3}$ for $\omega \ll \omega_c$ (see Eq.(11)); in order to make the radiation from the electrons at $x = 0$ and $x = L$ coherent, the condition $L \ll \rho\theta_c$ needs to be satisfied. Therefore, the upper limit of the coherent frequency is given by

$$\omega_m \sim \left(\frac{\rho}{L} \right)^2 \omega_l. \quad (24)$$

Any electromagnetic wave with $\omega \gg \omega_m$ would not be coherent. In summary, one has

$$F_\omega(N) \simeq \begin{cases} N^2 & \omega \ll \omega_l \\ N^2 \left(\frac{\omega}{\omega_l} \right)^{-2} & \omega_l \ll \omega \ll \omega_m \end{cases}. \quad (25)$$

FIG. 3.— F_ω - ω relation, see Eq.(22).

The F_ω - ω relation is shown in Figure 3. If $\omega \ll \omega_l$, the wavelength of the electromagnetic waves will be much larger than the bunch length, which means that the radiation from each electron has almost the same phase. In this case, one has significant coherence. On the other hand, if $\omega \gtrsim \omega_l$, the factor of $\sin^2(\omega/\omega_l)/(\omega/\omega_l)^2$ will play a role to reduce coherence, which causes: 1. the maximum value of $F_\omega(N)$ proportional to ω^{-2} ; and 2. the spectral oscillation. At the frequency around $\sim \omega_l$, the spectrum oscillation is significant. For higher frequencies, e.g., $\omega \gg 10\omega_l$, since oscillation becomes rapid, the observed spectrum would appear as a power law. Finally, once $\omega \gg \omega_m$ is satisfied, the radiation will become incoherent.

4.1.2. More than one bunch in the trajectory

Next, we consider that there are N_B bunches in the trajectory. For each bunch, the length and the electron number are assumed to be L and N , respectively. We define that x_j is the distance between the j th electron and the first electron in each bunch, and s_n is the distance between the first electron in the n th bunch and the first electron in the first bunch. If the total length of N_B bunches, including the spaces between each bunch, is much less than the curvature radius ρ of the trajectory, then the angle between each bunch velocity and the line of sight is almost the same, e.g., $\varphi_n \sim \varphi$. Similar to the discussion in the above section, one has

$$\begin{aligned} F_\omega(N, N_B) &= \left| \sum_n^{N_B} \sum_j^N e^{-ik(x_j + s_n) \cos \varphi} \right|^2 \\ &= \left| \sum_n^{N_B} e^{-iks_n \cos \varphi} \right|^2 \left| \sum_j^N e^{-ikx_j \cos \varphi} \right|^2 \\ &= N^2 N_B^2 \left[\frac{\sin(\omega/\omega_l)}{(\omega/\omega_l)} \right]^2 \left[\frac{\sin(\omega/\omega_{bl})}{(\omega/\omega_{bl})} \right]^2 \end{aligned} \quad (26)$$

where $\omega_{bl} = 2c/s_{NB} \cos \varphi$. Define L_s is the mean space between each bunch, then $s_{NB} = (N_B - 1)(L + L_s)$. We also define the maximum bunch-coherent frequency, e.g.,

$$\omega_{bm} \sim \left(\frac{\rho}{s_{NB}} \right)^2 \omega_{bl}. \quad (27)$$

If $\omega \ll \omega_{bm}$, the superposition of the electromagnetic waves from each bunch will be coherent, and the radia-

tion energy is corrected by the factor of Eq.(26). However, if $\omega > \omega_{bm}$, Eq.(26) is not applicable. In this case, the superposition of the electromagnetic waves from different bunches will not be coherent, one may have $F_\omega(N, N_B) \sim N_B F_\omega(N)$, where $F_\omega(N)$ corresponds to one bunch.

As shown in Figure 3, for one bunch, the spectrum appears a significant oscillation at ω_l , which can show the discrete band structure in the spectrum. Such a property might explain the narrow spectrum of the nanosecond giant pulse of the Crab pulsar (Hankins & Eilek 2007). However, for more than one bunch, if the time intervals of each bunch satisfies random distribution, the oscillation in the total spectrum would be smoothed.

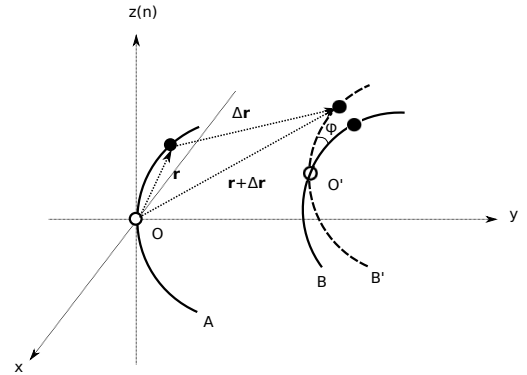
4.1.3. Steady current flowing in the entire trajectory

Assuming that the electrons are distributed in the entire trajectory, and the charge density and the current density are independent of time. According to Maxwell's equation, the electromagnetic field generated by a steady source is steady, which can not contribute to radiation, i.e.,

$$\left. \frac{dI_{\text{current}}}{d\omega d\Omega} \right|_{\text{steady}} = 0. \quad (28)$$

In general, a current can be considered to consist of a steady component and some perturbations. Only the fluctuating net charges in these perturbations can contribute to coherent radiation.

4.2. Electrons in the trajectory family

FIG. 4.— A trajectory (B) generated via displacement ($A \rightarrow B'$) and rotation ($B' \rightarrow B$) by the “seed” trajectory (A).

If the charges are not in the same trajectory, a detailed calculation of the coherent emission will be complex. We consider the following “simplified trajectory-family assumption”: 1. electrons are in the different trajectories with the same curvature radius; 2. at the retarded time $t = 0$, all the electrons are in the plane perpendicular to the line of sight. Under the above conditions, we consider the appropriate coordinate system in Figure 4, where all electrons are in the $x - y$ plane at retarded time $t = 0$, the direction of the line of sight is along the z axis.

As shown in Figure 4, for any trajectory in the above condition, like the B trajectory, it can be generated via “rotation” (around x , y or z axis) and “displacement” (in

the $x-y$ plane) by a “seed” trajectory, like the A trajectory, which is in the $y-z$ plane with the corresponding electron at the origin at $t=0$. Therefore, using the seed trajectory and the transformations, we can generate a family of trajectories. We consider the following basic trajectory families: 1. generated via rotation around z axis by the seed trajectory; 2. generated via rotation around y axis by the seed trajectory; 3. generated via rotation around x axis by the seed trajectory; 4. one of the above three cases adding a displacement.

First, we note that a displacement of a trajectory does not change its radiation spectrum. For a displacement, e.g., $\mathbf{r}(t) \rightarrow \mathbf{r}(t) + \Delta\mathbf{r}$ with $\mathbf{n} \cdot \Delta\mathbf{r} = 0$, one has

$$\begin{aligned} \beta &\rightarrow \beta, \\ \mathbf{n} \cdot \mathbf{r}(t) &\rightarrow \mathbf{n} \cdot (\mathbf{r}(t) + \Delta\mathbf{r}) = \mathbf{n} \cdot \mathbf{r}(t). \end{aligned} \quad (29)$$

According to Eq.(2), $dI/d\omega d\Omega$ remains unchanged under the displacement. Therefore, one can shift one trajectory in the plane perpendicular the line of sight and not change its observed spectrum⁵.

For example, if the N trajectories keep parallel to each other and satisfy the above simplified trajectory-family assumption, According to the displacement invariance, the corresponding energy radiated per unit solid angle per unit frequency interval is

$$\frac{dI_{(N)}}{d\omega d\Omega} = N^2 \frac{dI_{(1)}}{d\omega d\Omega}. \quad (30)$$

Since the displacement does not change the radiation, in the following we only need to consider the three rotation cases, i.e. the trajectory family is generated via: 1. rotation around the z axis; 2. rotation around the y axis; and 3. rotation around the x axis.

4.2.1. Family I: Generated via rotation around Z axis

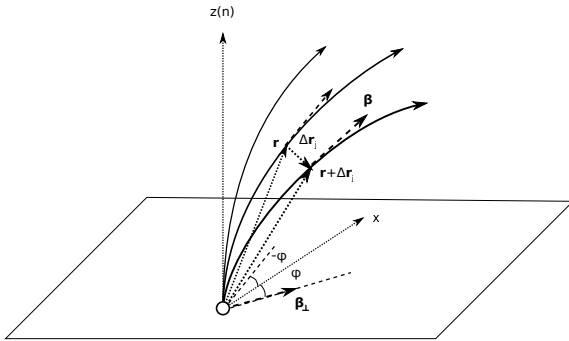


FIG. 5.— A trajectory family generated via rotation around z axis by the seed trajectory.

If the trajectory family is generated via the rotation around z axis, as shown in Figure 5, one has $\mathbf{n} \cdot \Delta\mathbf{r}_j = 0$ and $\mathbf{n} \cdot \mathbf{r}_j(t) = \mathbf{n} \cdot \mathbf{r}(t)$, where $\mathbf{r}(t)$ denotes the seed trajectory, leading to the same exponential term in Eq.(3) for each electron. Define $\beta_{\perp,j}$ as the component of β_j in the plane that is perpendicular to the line of sight, one has,

$$\mathbf{n} \times (\mathbf{n} \times \beta_j) = -\beta_{\perp,j}. \quad (31)$$

⁵ Note that the displacement invariance is based on the assumption that the scale of the accelerating region is much less than the distance between the source and the observer.

Next, for simplicity, we assume that the trajectory family is generated by rotating the seed trajectory (the median trajectory) by $\pm\varphi$, and there are N trajectories uniformly spaced in the opening angle 2φ . $\mathbf{r}(t)$ corresponds to the median trajectory, and φ_j corresponds to the angle between the j th trajectory and the median trajectory, as shown in Figure 5. Since the velocities of the electrons have the same z component, one can define $\beta_j = \beta(b \cos \varphi_j, b \sin \varphi_j, \sqrt{1-b^2})$, where $\beta\sqrt{1-b^2}$ corresponds to the z component. Therefore, one has $\mathbf{n} \times (\mathbf{n} \times \beta_j) = -\beta b(\cos \varphi_j, \sin \varphi_j, 0)$. The sum of $\mathbf{n} \times (\mathbf{n} \times \beta_j)$ in Eq.(3) is given by

$$\begin{aligned} \sum_{j=1}^N \mathbf{n} \times (\mathbf{n} \times \beta_j) &= \left(\frac{N}{2\varphi} \int_{-\varphi}^{\varphi} \cos \varphi' d\varphi' \right) (-\beta b) \hat{x} \\ &= \frac{\sin \varphi}{\varphi} N(-\beta_{\perp}), \end{aligned} \quad (32)$$

where $\beta_{\perp} = -\mathbf{n} \times (\mathbf{n} \times \beta)$ is the perpendicular component of β of the electron in the median trajectory. Finally, we have

$$\frac{dI_{(N)}}{d\omega d\Omega} = \frac{dI_{(1)}}{d\omega d\Omega} \left(\frac{\sin \varphi}{\varphi} \right)^2 N^2. \quad (33)$$

Note that if the trajectory family is axisymmetric, e.g., $\varphi = \pi$ (φ is the half-opening angle), the radiation energy would be zero.

4.2.2. Family II: Generated via rotation around Y axis

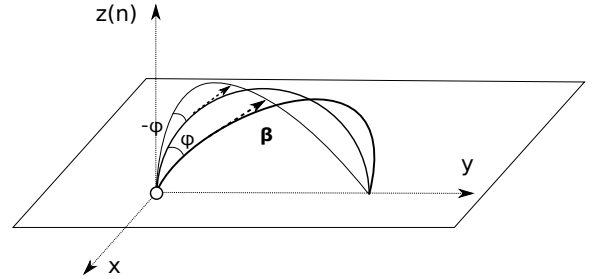


FIG. 6.— A trajectory family generated via rotation around y axis by the seed trajectory.

If the trajectory family is generated via the rotation around y axis, the radiation amplitude of one trajectory in the trajectory family can be calculated following Section 3.1, with the observation angle θ replaced by $\theta + \varphi_j$, where φ_j corresponds to the angle between the j th trajectory and the median trajectory. We assume that the bunch opening angle of the N trajectories is 2φ , and each trajectory is uniformly spaced within the bunch opening angle. The detailed calculation can be found in Appendix C. First, we consider that there is only one electron in each trajectory, and all electrons have the same Lorentz factor γ . We define

$$\omega_{\varphi} = \frac{3c}{\rho\varphi^3}. \quad (34)$$

According to Appendix C, if $\omega > \omega_{\varphi}$, only a part of radiation within the bunch opening angle will be coherent. However, if $\omega < \omega_{\varphi}$, the radiation from the entire bunch opening angle will be coherent, as shown in Figure 7.

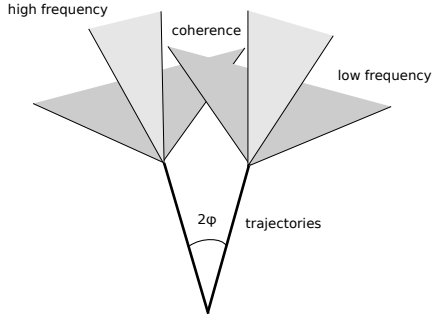


FIG. 7.— Coherent curvature radiation from a bunch opening angle. Dark grey beam denotes low-frequency radiation, and light grey beam denotes high-frequency radiation. If $\omega > \omega_\varphi$, only a part of radiation in the bunch opening angle will be coherent. If $\omega < \omega_\varphi$, the radiation from the entire bunch opening angle will be coherent.

For $\omega_\varphi < \omega_c$, the energy radiated per unit frequency interval per unit solid angle is given by (see Appendix C)

$$\frac{dI}{d\omega d\Omega} = \frac{e^2}{c} \frac{3}{2^{4/3}} \left[\frac{\Gamma(2/3)}{\pi} \right]^2 N^2 \gamma^2 \times \begin{cases} \left(\frac{\omega}{\omega_c} \right)^{2/3} & \omega \ll \omega_\varphi \\ \left(\frac{\omega_\varphi}{\omega_c} \right)^{2/3} e^{-\omega/\omega_c} & \omega \gg \omega_\varphi \end{cases}. \quad (35)$$

For $\omega_\varphi > \omega_c$, all the radiation energy in the bunch opening angle can be observed, the radiation energy would be given by Eq.(10).

Next, we further consider that there are more than one electrons in a point source in each trajectory and the electron distribution satisfies the power-law distribution, e.g. $N_e(\gamma)d\gamma = N_{e,0}(\gamma/\gamma_1)^{-p}d\gamma$ for $\gamma_1 < \gamma < \gamma_2$. According to Appendix C, for $\omega_\varphi \ll \omega_{c1}$, the energy radiated per unit frequency interval per unit solid angle is given by

$$\frac{dI}{d\omega d\Omega} = \frac{e^2}{c} \frac{2^{(2p-6)/3}}{3\pi^2} \left[\Gamma\left(\frac{2}{3}\right) \Gamma\left(\frac{p-1}{3}\right) \right]^2 N_{e,0}^2 \gamma_1^4 \times \begin{cases} \left(\frac{\omega}{\omega_{c1}} \right)^{2/3} & \omega \ll \omega_\varphi \\ \left(\frac{\omega_\varphi}{\omega_{c1}} \right)^{2/3} & \omega_\varphi \ll \omega \ll \omega_{c1} \\ \left(\frac{\omega_\varphi}{\omega_{c1}} \right)^{2/3} \left(\frac{\omega}{\omega_{c1}} \right)^{-(2p-2)/3} & \omega \gg \omega_{c1} \end{cases}. \quad (36)$$

For $\omega_\varphi \gg \omega_{c1}$, the energy radiated per unit frequency

interval per unit solid angle is given by

$$\frac{dI}{d\omega d\Omega} = \frac{e^2}{c} \frac{2^{(2p-6)/3}}{3\pi^2} \left[\Gamma\left(\frac{2}{3}\right) \Gamma\left(\frac{p-1}{3}\right) \right]^2 N_{e,0}^2 \gamma_1^4 \times \begin{cases} \left(\frac{\omega}{\omega_{c1}} \right)^{2/3} & \omega \ll \omega_{c1} \\ \left(\frac{\omega}{\omega_{c1}} \right)^{-(2p-4)/3} & \omega_{c1} \ll \omega \ll \omega_\varphi \\ \left(\frac{\omega_\varphi}{\omega_{c1}} \right)^{-(2p-4)/3} \left(\frac{\omega}{\omega_\varphi} \right)^{-(2p-2)/3} & \omega \gg \omega_\varphi \end{cases}. \quad (37)$$

4.2.3. Family III: Generated via rotation around X axis

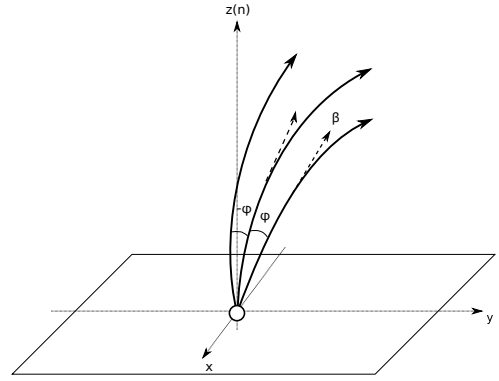


FIG. 8.— A trajectory family generated via rotation around x axis by the seed trajectory.

Finally, we consider that the trajectory family generated via the rotation around x axis. We also assume that the bunch opening angle of the N trajectories is 2φ , and each trajectory is uniformly spaced in the bunch opening angle, as shown in Figure 8. In this case, the radiation spectrum will be as same as Family II (see Appendix D). For the monoenergetic electron distribution, the radiation energy is given by Eq.(35) and Eq.(10). For the power-law electron distribution, the radiation energy is given by Eq.(36) and Eq.(37). The detailed calculation is shown in Appendix D.

4.3. Electrons in the trajectories with different curvature radii

In the above discussions, we have assumed that all the trajectories have the same curvature radius. If the trajectories have different curvature radii, the spectrum of coherent radiation will be more complex. We discuss the simplest case: two electrons are at the origin at the retarded time $t = 0$, and their trajectories lie in the same plane and have the same orientation. Assume that the two electrons have the same energy γ and the curvature radii of each trajectory are ρ_1 and ρ_2 , respectively. The corresponding critical frequencies are $\omega_{c1} = 3c\gamma^3/2\rho_1$ and $\omega_{c2} = 3c\gamma^3/2\rho_2$, respectively. The electromagnetic waves at the critical frequencies are $\mathbf{E}_1 = \mathbf{E}_{01}e^{i\omega_{c1}t}$ and $\mathbf{E}_2 = \mathbf{E}_{02}e^{i\omega_{c2}t}$, respectively. According to Eq.(6) and Eq.(A1), the amplitude \mathbf{E}_0 is proportional to the curvature radius ρ . We define $\Delta\rho = \rho_2 - \rho_1$, $\rho = (\rho_1 + \rho_2)/2$, $\Delta\omega_c = \omega_{c2} - \omega_{c1}$,

$\omega_c = (\omega_{c1} + \omega_{c2})/2$, and $\mathbf{E}_0 = (\mathbf{E}_{01} + \mathbf{E}_{02})/2$. For $\Delta\rho \lesssim \rho$, the superposition of both waves is given by

$$\begin{aligned} \mathbf{E} &= \mathbf{E}_1 + \mathbf{E}_2 = \mathbf{E}_{01}e^{i\omega_{c1}t} + \mathbf{E}_{02}e^{i\omega_{c2}t} \\ &\simeq \mathbf{E}_0 (1 + e^{i\Delta\omega_c t}) e^{i\omega_c t}. \end{aligned} \quad (38)$$

Thus, the amplitude of the superposition is

$$\mathbf{E}_b \equiv \mathbf{E}_0 (1 + e^{i\Delta\omega_c t}), \quad (39)$$

with the period of

$$T_b = \frac{2\pi}{\Delta\omega_c} \simeq \frac{4\pi\rho^2}{3c\gamma^3\Delta\rho}. \quad (40)$$

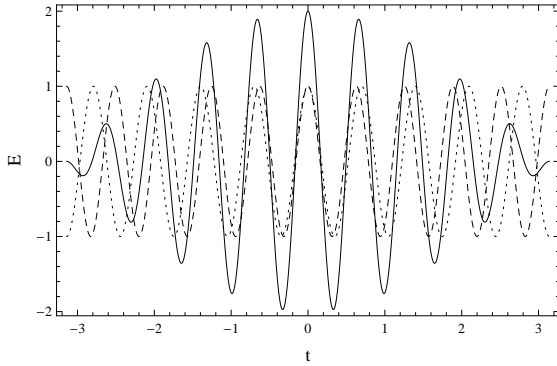


FIG. 9.— Wave beat: the dashed and dotted lines denote the wave with frequencies ω_{c1} and ω_{c2} , respectively, and the solid line denotes the superposition of two waves.

Such an effect is called as “wave beat”. As shown in Figure 9, for the first-half period with $-T_b/4 < t < T_b/4$, the amplitude of the coherent wave satisfies $\mathbf{E}_0 < \mathbf{E}_b < 2\mathbf{E}_0$. For the second-half period with $T_b/4 < t < T_b/2$ and $-T_b/2 < t < -T_b/4$, the amplitude of the coherent wave satisfies $0 < \mathbf{E}_b < \mathbf{E}_0$. During the entire beat period T_b , the mean amplitude of the coherent wave is \mathbf{E}_0 . In order to make the superposition coherently enhanced, the pulse duration T_p (See Eq. (13)) of the curvature radiation should be much less than the half period $T_b/2$, e.g., $T_p \ll T_b/2$. Therefore, the coherent condition of the trajectories with different curvature radii is

$$\Delta\rho \ll \frac{4\pi}{3}\rho \left(\frac{\omega}{2\omega_c} \right)^{1/3}. \quad (41)$$

5. CURVATURE RADIATION FROM A THREE-DIMENSIONAL BUNCH

In this section, we consider that the curvature radiation from a three-dimensional bunch characterized by the following parameters: the electron energy distribution $N_e(\gamma)d\gamma$, the curvature radius of the trajectory family ρ (In order to make the wave coherent, the difference of the curvature radii of the trajectories is required to be very small, see Section 4.3), the bunch length L , and a pair of the orthogonal bunch opening angles $(\varphi_\times, \varphi_+)$ with their centers pointing to the observer, as shown in Figure 10.

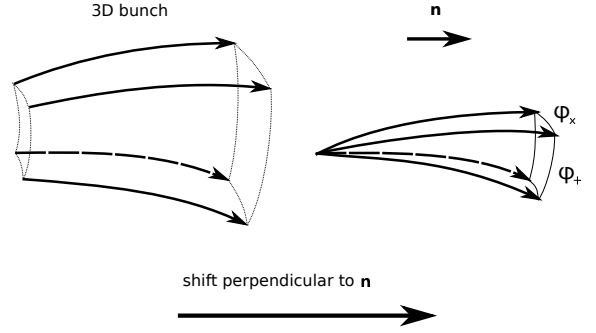


FIG. 10.— Left panel: A three-dimensional bunch characterized by: bunch length, curvature radius and bunch opening angles of the trajectory family. Right panel: Displacement transformation (perpendicular to the line of sight) from the left panel.

According to the displacement invariance. e.g., Eq. (29), we can gather the trajectories in the plane perpendicular to the line of sight, see Figure 10. In the simplest case, we assume that the electrons are uniformly distributed in L and $(\varphi_\times, \varphi_+)$, then such a three-dimensional bunch can be treated as the combination of one-dimensional bunch (see Section 4.1) and two of the three rotation cases (see Section 4.2).

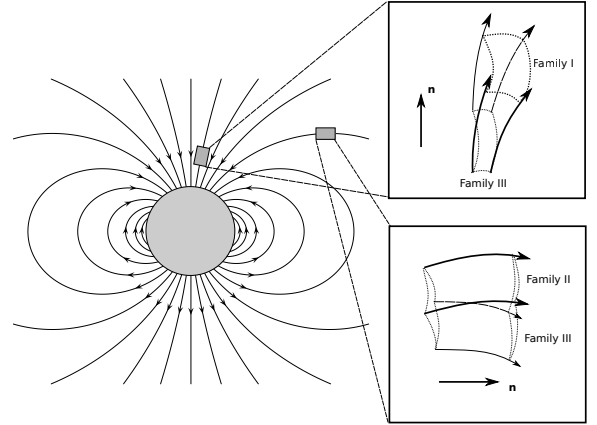


FIG. 11.— Two typical magnetic field configurations of a three-dimensional bunch in the magnetosphere. Top-right panel: the field configuration in the bunch is consist of Family I and Family III. Bottom-right panel: the field configuration in the bunch is consist of Family II and Family III.

For curvature radiation, due to the strong magnetic fields in the magnetosphere near a neutron star, the bunch will move along with the field line. Thus, the trajectories overlap with the field lines. We consider two typical magnetic field configurations for a three-dimensional bunch, as shown in Figure 11. In the case of the top-right panel in Figure 11, the emission region is close to the magnetic axis of the dipole field, and the field configuration in the bunch consists of Family I and Family III, as discussed in Section 4.2⁶. In the case of the bottom-right panel in Figure 11, the emission region is near the region where the field is perpendicular to the magnetic axis. The field configuration in the bunch con-

⁶ Strictly speaking the field configuration consists of Family I and Family III, only when the emission region is at the center of the dipole field. However, for an emission region close to the magnetic axis, the approximation is reasonable.

sists of Family II and Family III. In the above two cases, φ_{\times} and φ_{+} correspond to the bunch opening angle of the corresponding cases, respectively.

5.1. Family A: combination of Family I and Family III

At first, we consider the case that the emission region is close to the magnetic axis, as shown in the top-right panel of Figure 11. In this case, the pair of the orthogonal bunch opening angles $(\varphi_{\times}, \varphi_{+})$ are (φ_1, φ) , where φ_1 and φ are the bunch opening angles of Family I and Family III field lines, respectively. We also define

$$K(p) \equiv \frac{2^{(2p-6)/3}}{3\pi^2} \left[\Gamma\left(\frac{2}{3}\right) \Gamma\left(\frac{p-1}{3}\right) \right]^2. \quad (42)$$

Without loss of generality, we consider that the upper limit of the frequency, e.g., $\min(\omega_m, \omega_{c2})$, is much larger than other typical frequencies. According to Section 4.1.1, Section 4.2.1 and Section 4.2.3, using Eq.(19), Eq.(25), Eq.(33), Eq.(36) and Eq.(37), the energy radiated per unit frequency interval per unit solid angle could be given by the following formulas.

A. For $\omega_{\varphi} \ll \omega_{c1}$:

(a) If $\omega_l \ll \omega_{\varphi} \ll \omega_{c1}$, the spectrum is shown in the panel (a) of Figure 12, and one has

$$\begin{aligned} \frac{dI}{d\omega d\Omega} = & K(p) \frac{e^2}{c} N_{e,0}^2 \gamma_1^4 \left(\frac{\sin \varphi_1}{\varphi_1} \right)^2 \\ & \times \begin{cases} \left(\frac{\omega}{\omega_{c1}} \right)^{2/3} & \omega \ll \omega_l \\ \left(\frac{\omega_l}{\omega_{c1}} \right)^{2/3} \left(\frac{\omega}{\omega_l} \right)^{-4/3} & \omega_l \ll \omega \ll \omega_{\varphi} \\ \left(\frac{\omega_l}{\omega_{c1}} \right)^{2/3} \left(\frac{\omega_{\varphi}}{\omega_l} \right)^{-4/3} \left(\frac{\omega}{\omega_{\varphi}} \right)^{-2} & \omega_{\varphi} \ll \omega \ll \omega_{c1} \\ \left(\frac{\omega_l}{\omega_{c1}} \right)^{2/3} \left(\frac{\omega_{\varphi}}{\omega_l} \right)^{-4/3} \left(\frac{\omega_{c1}}{\omega_{\varphi}} \right)^{-2} \left(\frac{\omega}{\omega_{c1}} \right)^{-(2p+4)/3} & \omega \gg \omega_{c1} \end{cases} \end{aligned} \quad (43)$$

(b) If $\omega_{\varphi} \ll \omega_l \ll \omega_{c1}$, the spectrum is shown in the panel (b) of Figure 12, and one has

$$\begin{aligned} \frac{dI}{d\omega d\Omega} = & K(p) \frac{e^2}{c} N_{e,0}^2 \gamma_1^4 \left(\frac{\sin \varphi_1}{\varphi_1} \right)^2 \\ & \times \begin{cases} \left(\frac{\omega}{\omega_{c1}} \right)^{2/3} & \omega \ll \omega_{\varphi} \\ \left(\frac{\omega_{\varphi}}{\omega_{c1}} \right)^{2/3} & \omega_{\varphi} \ll \omega \ll \omega_l \\ \left(\frac{\omega_{\varphi}}{\omega_{c1}} \right)^{2/3} \left(\frac{\omega}{\omega_l} \right)^{-2} & \omega_l \ll \omega \ll \omega_{c1} \\ \left(\frac{\omega_{\varphi}}{\omega_{c1}} \right)^{2/3} \left(\frac{\omega_{c1}}{\omega_l} \right)^{-2} \left(\frac{\omega}{\omega_{c1}} \right)^{-(2p+4)/3} & \omega \gg \omega_{c1} \end{cases} \end{aligned} \quad (44)$$

(c) If $\omega_{\varphi} \ll \omega_{c1} \ll \omega_l$, the spectrum is shown in the panel (c) of Figure 12, and one has

$$\begin{aligned} \frac{dI}{d\omega d\Omega} = & K(p) \frac{e^2}{c} N_{e,0}^2 \gamma_1^4 \left(\frac{\sin \varphi_1}{\varphi_1} \right)^2 \\ & \times \begin{cases} \left(\frac{\omega}{\omega_{c1}} \right)^{2/3} & \omega \ll \omega_{\varphi} \\ \left(\frac{\omega_{\varphi}}{\omega_{c1}} \right)^{2/3} & \omega_{\varphi} \ll \omega \ll \omega_{c1} \\ \left(\frac{\omega_{\varphi}}{\omega_{c1}} \right)^{2/3} \left(\frac{\omega}{\omega_{c1}} \right)^{-(2p-2)/3} & \omega_{c1} \ll \omega \ll \omega_l \\ \left(\frac{\omega_{\varphi}}{\omega_{c1}} \right)^{2/3} \left(\frac{\omega_l}{\omega_{c1}} \right)^{-(2p-2)/3} \left(\frac{\omega}{\omega_l} \right)^{-(2p+4)/3} & \omega \gg \omega_l \end{cases} \end{aligned} \quad (45)$$

B. For $\omega_{\varphi} \gg \omega_{c1}$:

(a) If $\omega_l \ll \omega_{c1} \ll \omega_{\varphi}$, the spectrum is shown in the panel (a) of Figure 13, and one has

$$\begin{aligned} \frac{dI}{d\omega d\Omega} = & K(p) \frac{e^2}{c} N_{e,0}^2 \gamma_1^4 \left(\frac{\sin \varphi_1}{\varphi_1} \right)^2 \\ & \times \begin{cases} \left(\frac{\omega}{\omega_{c1}} \right)^{2/3} & \omega \ll \omega_l \\ \left(\frac{\omega_l}{\omega_{c1}} \right)^{2/3} \left(\frac{\omega}{\omega_l} \right)^{-4/3} & \omega_l \ll \omega \ll \omega_{c1} \\ \left(\frac{\omega_l}{\omega_{c1}} \right)^2 \left(\frac{\omega}{\omega_{c1}} \right)^{-(2p+2)/3} & \omega_{c1} \ll \omega \ll \omega_{\varphi} \\ \left(\frac{\omega_l}{\omega_{c1}} \right)^2 \left(\frac{\omega_{\varphi}}{\omega_{c1}} \right)^{-(2p+2)/3} \left(\frac{\omega}{\omega_{\varphi}} \right)^{-(2p+4)/3} & \omega \gg \omega_{\varphi} \end{cases} \end{aligned} \quad (46)$$

(b) If $\omega_{c1} \ll \omega_l \ll \omega_{\varphi}$, the spectrum is shown in the panel (b) of Figure 13, and one has

$$\begin{aligned} \frac{dI}{d\omega d\Omega} = & K(p) \frac{e^2}{c} N_{e,0}^2 \gamma_1^4 \left(\frac{\sin \varphi_1}{\varphi_1} \right)^2 \\ & \times \begin{cases} \left(\frac{\omega}{\omega_{c1}} \right)^{2/3} & \omega \ll \omega_{c1} \\ \left(\frac{\omega}{\omega_{c1}} \right)^{-(2p-4)/3} & \omega_{c1} \ll \omega \ll \omega_l \\ \left(\frac{\omega_l}{\omega_{c1}} \right)^{-(2p-4)/3} \left(\frac{\omega}{\omega_l} \right)^{-(2p+2)/3} & \omega_l \ll \omega \ll \omega_{\varphi} \\ \left(\frac{\omega_l}{\omega_{c1}} \right)^{-(2p-4)/3} \left(\frac{\omega_{\varphi}}{\omega_l} \right)^{-(2p+2)/3} \left(\frac{\omega}{\omega_{\varphi}} \right)^{-(2p+4)/3} & \omega \gg \omega_{\varphi} \end{cases} \end{aligned} \quad (47)$$

(c) If $\omega_{c1} \ll \omega_{\varphi} \ll \omega_l$, the spectrum is shown in the

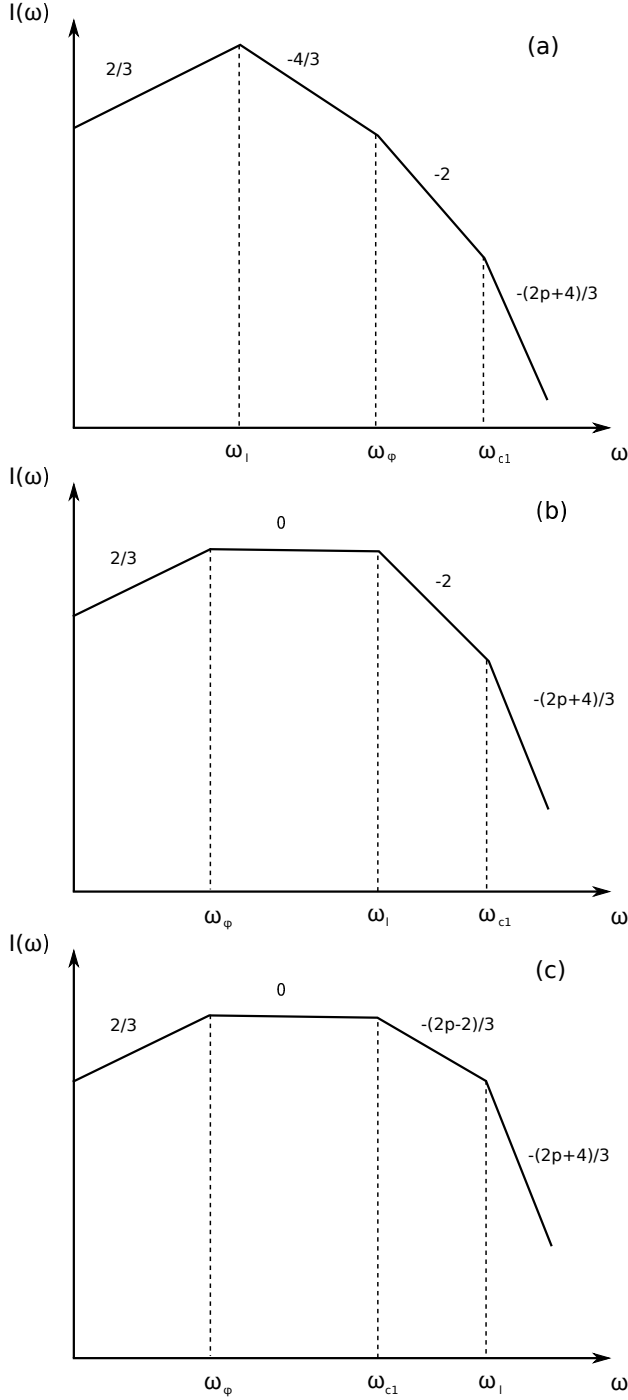


FIG. 12.— The spectra of the coherent curvature radiation from a three-dimensional bunch: (a) the spectrum with $\omega_l \ll \omega_\phi \ll \omega_{c1}$; (b) the spectrum with $\omega_\phi \ll \omega_l \ll \omega_{c1}$; (c) the spectrum with $\omega_\phi \ll \omega_{c1} \ll \omega_l$.

panel (c) of Figure 13, and one has

$$\frac{dI}{d\omega d\Omega} = K(p) \frac{e^2}{c} N_{e,0}^2 \gamma_1^4 \left(\frac{\sin \varphi_1}{\varphi_1} \right)^2 \times \begin{cases} \left(\frac{\omega}{\omega_{c1}} \right)^{2/3} & \omega \ll \omega_{c1} \\ \left(\frac{\omega}{\omega_{c1}} \right)^{-(2p-4)/3} & \omega_{c1} \ll \omega \ll \omega_\phi \\ \left(\frac{\omega_\phi}{\omega_{c1}} \right)^{-(2p-4)/3} \left(\frac{\omega}{\omega_\phi} \right)^{-(2p-2)/3} & \omega_\phi \ll \omega \ll \omega_l \\ \left(\frac{\omega_\phi}{\omega_{c1}} \right)^{-(2p-4)/3} \left(\frac{\omega_l}{\omega_\phi} \right)^{-(2p-2)/3} \left(\frac{\omega}{\omega_l} \right)^{-(2p+4)/3} & \omega \gg \omega_l \end{cases} \quad (48)$$

5.2. Family B: combination of Family II and Family III

Next, we consider the emission region is near the region where the field is perpendicular to the magnetic axis, as shown in the bottom-right panel of Figure 11. In this case, the pair of the orthogonal bunch opening angles (φ_-, φ_+) are (φ_2, φ_3) , where φ_2 and φ_3 are the bunch opening angles of Family II and Family III, respectively. Noticing that the spectral properties of Family II and Family III field lines are the same, we define⁷

$$\varphi = \max(\varphi_2, \varphi_3). \quad (49)$$

According to Section 4.1.1, Section 4.2.2 and Section 4.2.3, using Eq.(19), Eq.(25), Eq.(36) and Eq.(37), the energy radiated per unit frequency interval per unit solid angle has the same form with Family A without a factor of $(\sin \varphi_1 / \varphi_1)^2$, i.e.

$$\left. \frac{dI}{d\omega d\Omega} \right|_{\text{Family B}} = \left(\frac{\sin \varphi_1}{\varphi_1} \right)^{-2} \left. \frac{dI}{d\omega d\Omega} \right|_{\text{Family A}} \quad (50)$$

where the subscript “Family A” corresponds to the results in Section 5.1.

6. APPLICATION TO PULSARS

6.1. General considerations

In general, the observed duration of one pulse from pulsars (also for fast radio bursts), e.g., $T_{\text{obs}} \sim 1$ ms, is much longer than the pulse duration of the curvature radiation, e.g., $T_p \sim 1/\nu_c \sim 1$ ns ($\nu_c/1$ GHz) (see Eq.(13)), which means that there must be more than one bunch sweeping cross the line of sight during the observed duration T_{obs} . The distance between the first bunch and the last bunch is $s_{NB} \sim cT_{\text{obs}} \sim 3 \times 10^7$ cm ($T_{\text{obs}}/1$ ms). According to Section 4.1.2, the maximum bunch-coherent frequency is $\omega_{bm} \sim (\rho/s_{NB})^2 \omega_{bl} \sim 2 \times 10^8$ rad s⁻¹ ($T_{\text{obs}}/1$ ms)⁻³ ($\rho/10^{10}$ cm)², where $\omega_{bl} \sim 2c/s_{NB}$. For the GHz radio wave, one has $\omega > \omega_{bm}$, which means that the superposition of the electromagnetic waves from each bunch is not coherent. Therefore,

⁷ Note that the quantity φ here is different from that of Family A in Section 5.1 (for Family A, φ is defined as the opening angle of Family III).

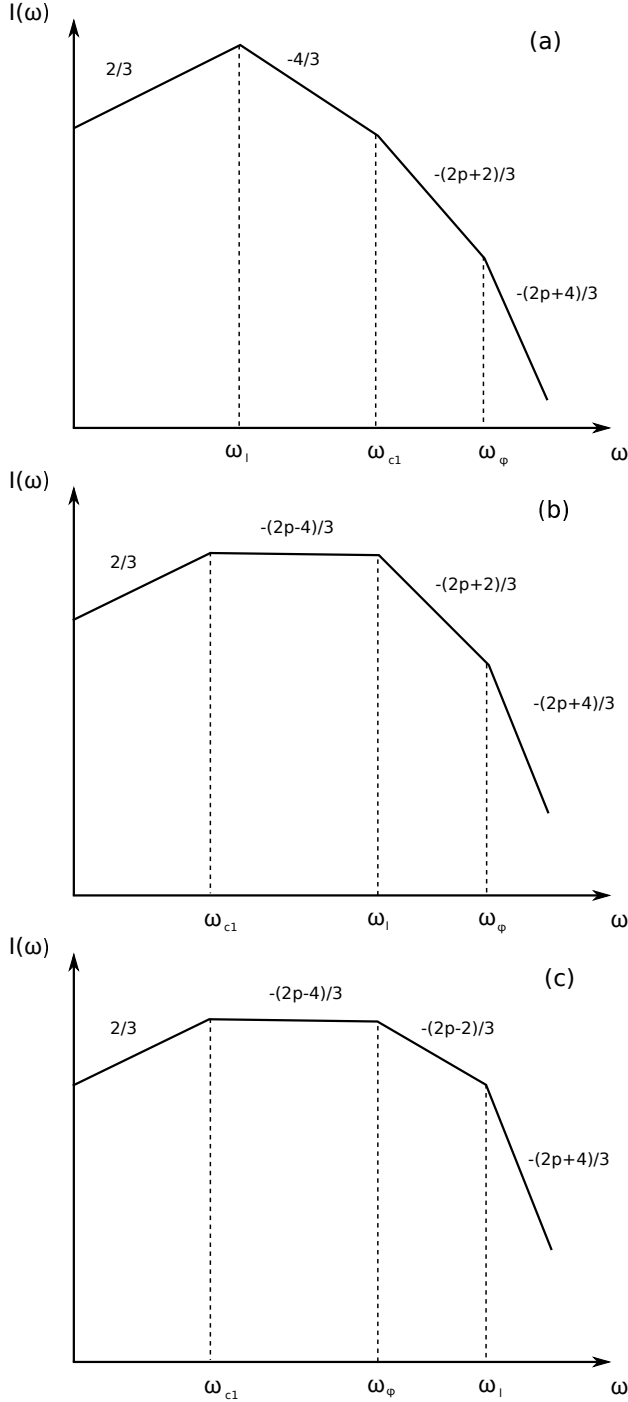


FIG. 13.— The spectra of the coherent curvature radiation from a three-dimensional bunch: (a) the spectrum with $\omega_l \ll \omega_{cl} \ll \omega_\phi$; (b) the spectrum with $\omega_{cl} \ll \omega_l \ll \omega_\phi$; (c) the spectrum with $\omega_{cl} \ll \omega_\phi \ll \omega_l$.

according to Eq.(4), the observed flux, the energy received per unit time per unit frequency per unit area, is given by

$$F_\nu = \frac{2\pi}{TD^2} \frac{dI}{d\omega d\Omega}, \quad (51)$$

where the factor of 2π is from the relation $F_\nu = 2\pi F_\omega$, and T is the mean time interval of each bunch, which corresponds to the gap between two adjacent bunches. Since the bunches might originate from

the abrupt discharges of the inner gaps near the neutron star surface (Ruderman & Sutherland 1975; Zhang et al. 1997; Gil & Sendyk 2000; Gil et al. 2006), instabilities of the outflow (Ruderman & Sutherland 1975; Egorenkov et al. 1983; Gedalin et al. 2002; Kumar et al. 2017; Lu & Kumar 2017), or the oscillation of acceleration region (Levinson et al. 2005; Beloborodov & Thompson 2007; Luo & Melrose 2008), it is reasonable to assume that the scale of the gap between adjacent bunches is of the order of the bunch scale, leading to $T \sim L/c$.

Before performing more quantitative estimates, we briefly discuss the possible mechanisms to form and maintain bunches. For a rotating magnetosphere, a continuous charged outflow is likely launched from the open field-line regions (Goldreich & Julian 1969). We consider that there are many bunches generated and dispersed in the emission region (e.g. Ruderman & Sutherland 1975). The bunch might disperse in a very short time T_d due to Coulomb repulsion (Cheng & Ruderman 1977) and velocity spread. This has been regarded as a main argument against the bunching mechanism as the coherent emission mechanisms of pulsars (e.g. Melrose 1978). However, if the generation time of a bunch is much shorter than T_{obs} , so that there would be always enough bunches being generated while being dispersed during the observed time scale, then one could observe bunched coherent radiation at any epoch. The continuous generation of such bunches may be tied to “sparking” discharges of the inner gap (Ruderman & Sutherland 1975; Zhang & Qiao 1996; Gil & Sendyk 2000; Gil et al. 2006) or the oscillating polar gaps (Luo & Melrose 2008). In these cases, the outflow from the polar cap region would deviates from the Goldreich-Julian density in a quasi-periodic manner, leading to bunches. In these cases, the fluctuating net charge density of one bunch would not be greater than the localized Goldreich-Julian density.

6.2. Curvature radiation from a dipole magnetosphere

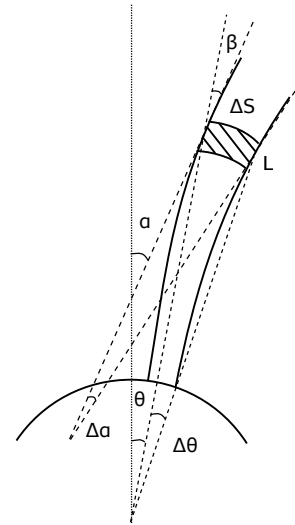


FIG. 14.— Curvature radiation from the dipole magnetosphere. The shadow area denotes a bunch with length L and cross section ΔS . θ is the poloidal angle of the dipole field, and α denotes the angle between the magnetic axis and the magnetic field. The emission region is close to the magnetic axis.

First, we consider that the emission region is close to the magnetic axis of a dipole field, as shown in Figure 14. A bunch, with the length L and the bunch opening angles $(\Delta\phi, \Delta\alpha)$, moves along the field lines. The bunch opening angles $(\Delta\phi, \Delta\alpha)$ are determined by the magnetic field configuration in the bunch, where α denotes the angle between the magnetic axis and the magnetic field, and ϕ denotes the toroidal angle of the dipole field. In this case, the magnetic field configuration is consistent with the Family A, and the spectrum is described in Section 5.1. For a given observed direction θ (the poloidal angle of the dipole field) and curvature radius ρ , the emission region (r, θ) can be determined by the magnetosphere geometry (see Appendix E), one has

$$r \simeq \frac{3}{4}\rho \sin \theta \quad \text{for} \quad \theta \lesssim 0.5 \quad (52)$$

In this case, according to Section 5.1 and Eq.(51), the observed flux, the energy received per unit time per unit frequency per unit area, at the peak frequency ν_{peak} is given by

$$\begin{aligned} F_{\nu, \text{max}} &= \frac{2\pi}{TD^2} \left. \frac{dI}{d\omega d\Omega} \right|_{\text{max}} \\ &\simeq \frac{2\pi e^2}{c} K(p) \frac{N_{e,0}^2 \gamma_1^4}{D^2 T} \left(\frac{\sin \Delta\phi}{\Delta\phi} \right)^2 \left(\frac{\nu_{\text{peak}}}{\nu_{c1}} \right)^{2/3}, \end{aligned} \quad (53)$$

where the peak frequency is given by $\nu_{\text{peak}} = \min(\nu_l, \nu_\varphi, \nu_{c1})$, where

$$\nu_l = \frac{c}{\pi L}, \quad \nu_\varphi = \frac{3c}{2\pi\rho(\Delta\alpha/2)^3}, \quad \nu_{c1} = \frac{3c\gamma_1^3}{4\pi\rho}. \quad (54)$$

Note that ν_φ is defined in Family A. As discussed in Section 3.3 and Section 4.1.3, only the fluctuating net charges in the Goldreich-Julian outflow can make the contribution to the coherent radiation. We define the effective electron number as $N_{e,\text{eff}}$, which corresponds to the fluctuating net charge number in a bunch. The net charge density of the bunch is $n_{\text{bun}} = n_{\text{GJ}} + \delta n_{\text{GJ}} \equiv (1 + \mu_c)n_{\text{GJ}}$, where $n_{\text{GJ}} = (\Omega B_p / 2\pi ec)(r/R)^{-3}$ is the Goldreich-Julian density (Goldreich & Julian 1969), B_p is the magnetic field strength at the polar cap, R is the neutron star radius, Ω is the angle velocity of the neutron star, and

$$\mu_c \equiv \frac{\delta n_{\text{GJ}}}{n_{\text{GJ}}} \quad (55)$$

is the normalized fluctuating net charge density δn_{GJ} that contributes to the coherent radiation. Here, we have assumed that the magnetic axis is parallel to the rotation axis. Therefore, for a power-law distribution of the effective electron number, e.g., $N_e(\gamma)d\gamma = N_{e,0}(\gamma/\gamma_1)^{-p}d\gamma$ with $N_{e,\text{eff}} = \int N_e(\gamma)d\gamma$, the effective electron number in the bunch volume V is given by

$$N_{e,\text{eff}} = \gamma_1 N_{e,0} / (p-1) = \mu_c n_{\text{GJ}} V. \quad (56)$$

The normalization of the electron distribution is given by

$$N_{e,0} = (p-1)\gamma_1^{-1}\mu_c n_{\text{GJ}} V. \quad (57)$$

As shown in Figure 14, according to the dipole magnetosphere geometry (see Appendix E), the bunch volume with the length L and the bunch opening angles $(\Delta\phi, \Delta\alpha)$ can be approximately given by

$$V = L\Delta S \simeq Lr^2 \frac{\sin \theta}{\cos \beta} \Delta\theta \Delta\phi \simeq \frac{2}{3} Lr^2 \sin \theta \Delta\alpha \Delta\phi, \quad (58)$$

where ΔS denotes the cross section, and β is the angle between the radial direction and the magnetic field, which is given by Eq.(E6). The relation between $\Delta\alpha$ and $\Delta\theta$ is given by Eq.(E9).

Next, we constrain $\Delta\alpha$ and $\Delta\phi$. In order to make the electromagnetic waves from the field lines with different curvature radii coherent, according to Eq.(41), the difference of the curvature radii should satisfy $\Delta\rho \ll \rho$ for $\omega \lesssim \omega_c$. For a given field line length l (from the dipole center to the emission region), the curvature radius at θ is approximately $\rho \sim 8l/3\theta$ (see Eq.(E5) in Appendix E), leading to $\Delta\theta/\theta \sim \Delta\rho/\rho \ll 1$. Using the relation $\Delta\alpha \sim (3/2)\Delta\theta$, the bunch opening angle $\Delta\alpha$ can be adopted as

$$\Delta\alpha \lesssim 0.1\alpha \sim 0.15\theta. \quad (59)$$

For $\Delta\alpha > 0.1\alpha \sim 0.15\theta$, the curvature radius would significantly change, which means that the electromagnetic waves from different field lines will not be coherent. On the other hand, different from $\Delta\alpha$, $\Delta\phi$ can be relatively larger. There are two reasons: 1. for a given poloidal angle θ , the field lines with different toroidal angle ϕ have the same curvature radius; 2. for a given (r, θ) , the angle between the magnetic field direction and the line of sight (the line of sight is taken to be tangent with the intermediate field line in the bunch opening angle), ψ , is always small, e.g.

$$\cos \psi = \cos \frac{\Delta\phi}{2} \sin^2 \alpha + \cos^2 \alpha \simeq 1 - \alpha^2 (1 - \cos \frac{\Delta\phi}{2}). \quad (60)$$

Therefore, even for a relatively large $\Delta\phi$, one always has $\psi \ll 1$ for $\alpha \simeq (3/2)\theta \ll 1$, leading to all the approximate conditions in the curvature radiation (ψ corresponds to θ in Section 3.1) being satisfied. Finally, the peak flux can be written as

$$\begin{aligned} F_{\nu, \text{max}} &= \frac{32(p-1)^2 K(p)}{81\pi c^2} \frac{\mu_c^2 \Omega^2 B_p^2 R^6 L \gamma_1^2 \Delta\alpha^2 \Delta\phi^2}{\rho^2 D^2} \\ &\times \left(\frac{\sin \Delta\phi}{\Delta\phi} \right)^2 \left(\frac{\nu_{\text{peak}}}{\nu_{c1}} \right)^{2/3}, \end{aligned} \quad (61)$$

where

$$\frac{\nu_{\text{peak}}}{\nu_{c1}} = \min \left(\frac{4\rho}{3L\gamma_1^3}, \frac{16}{\Delta\alpha^3 \gamma_1^3}, 1 \right). \quad (62)$$

There are three cases for the peak flux: Case I: for $\nu_{\text{peak}} = \nu_l$, one has

$$\begin{aligned} F_{\nu, \text{max}} &= \frac{32(p-1)^2 K(p)}{81\pi c^2} \left(\frac{4}{3} \right)^{2/3} \\ &\times \frac{\mu_c^2 \Omega^2 B_p^2 R^6 L^{1/3} \Delta\alpha^2 \Delta\phi^2}{\rho^{4/3} D^2} \left(\frac{\sin \Delta\phi}{\Delta\phi} \right)^2. \end{aligned} \quad (63)$$

Case II: for $\nu_{\text{peak}} = \nu_{\varphi}$, one has

$$F_{\nu, \text{max}} = \frac{2 \cdot 16^{5/3} (p-1)^2 K(p)}{81\pi c^2} \times \frac{\mu_c^2 \Omega^2 B_p^2 R^6 L \Delta \phi^2}{\rho^2 D^2} \left(\frac{\sin \Delta \phi}{\Delta \phi} \right)^2. \quad (64)$$

Case III: for $\nu_{\text{peak}} = \nu_{c1}$, one has

$$F_{\nu, \text{max}} = \frac{32(p-1)^2 K(p)}{81\pi c^2} \times \frac{\mu_c^2 \Omega^2 B_p^2 R^6 L \gamma_1^2 \Delta \alpha^2 \Delta \phi^2}{\rho^2 D^2} \left(\frac{\sin \Delta \phi}{\Delta \phi} \right)^2. \quad (65)$$

6.3. Model confronted with the pulsar data

Observationally, the spectra of pulsars can be fitted by a single power law, a two-segment broken power law, or a multi-segment broken power law (or log-parabolic) forms. Eighty percent of pulsars appear single power-law spectra. The spectral index is around $-(3-0)$ with the mean value of -1.6 (Lorimer et al. 1995; Jankowski et al. 2017). Seven percent of pulsars appear to have a two-segment broken power law. They show a mean spectral indices of -1.55 and -2.72 before and after the spectral break at ~ 1 GHz, with both indices having large scatter (Xilouris et al. 1996). Ten percent of pulsars can be fitted via a multi-segment broken power law or a log-parabolic spectral model (Jankowski et al. 2017). These spectra appear more complex than the above two classes.

As discussed in Section 5, the spectrum of the curvature radiation from a bunch moving in a three-dimensional field naturally predicts a multi-segment broken power law spectrum. The break frequencies are determined by the curvature radius, bunch length, and bunch opening angles. In general, the observed frequency band is narrow, which means that the observed spectra might be a part of a multi-segment broken power law. Thus, our model can naturally explain the observed spectra of pulsars.

For example, we consider the following typical parameters of a pulsar: $D = 5$ kpc, $R = 10^6$ cm, $B_p = 10^{12}$ G, and $P = 0.1$ s. We introduce a moderate fluctuation parameter $\mu_c = 0.1$. Other parameters are adopted as $L = 10$ cm, $\gamma_1 = 1000$, $\rho = 10^{10}$ cm, $p = 3$, $\theta = 0.01$, and $\Delta \phi = 0.1$. In this case, the distance from the emission region to the dipole field center is $r = 7.5 \times 10^7$ cm, the typical frequencies are $\nu_{c1} = 0.7$ GHz, $\nu_l = 0.9$ GHz, $\nu_{\varphi} = 3.4$ GHz, and the observed flux is $F_{\nu, \text{max}} = 2$ mJy. Due to $\nu_{c1} < \nu_l < \nu_{\varphi}$, the predict spectral index α_{index} is shown in the panel (b) of Figure 13: the spectral index is $\alpha_{\text{index}} \sim 0.7$ for $\nu \lesssim 0.7$ GHz; $\alpha_{\text{index}} \sim -0.7$ for $0.7 \text{ GHz} \lesssim \nu \lesssim 0.9$ GHz; $\alpha_{\text{index}} \sim -2.7$ for $0.9 \text{ GHz} \lesssim \nu \lesssim 3.4$ GHz; $\alpha_{\text{index}} \sim -3.3$ for $\nu \gtrsim 3.4$ GHz. Thus, for the above parameters, the spectrum shows a multi-segment broken law near ~ 1 GHz.

These are generally consistent with the pulsar data. For the pulsars with the observed spectra having a single power law and a two-segment broken power law, they can also be explained by this model as long as the break frequencies, e.g., ν_{c1} , ν_l and ν_{φ} , have relatively large separations so that within the observed frequency band only zero or one break are observable. These can be achieved with reasonable pulsar parameters.

7. APPLICATION TO FAST RADIO BURSTS

7.1. Model A: Spindown powered scenario

Fast radio bursts (FRBs) are mysterious radio transients characterized by millisecond-duration durations, large dispersion measure, and extremely high brightness temperature (e.g. Lorimer et al. 2007; Thornton et al. 2013; Chatterjee et al. 2017). Thanks to multi-wavelength follow-up observations and a precise localization (Chatterjee et al. 2017; Marcote et al. 2017), the repeating FRB, FRB 121102, was identified in a dwarf galaxy at $z = 0.19273$ (Tendulkar et al. 2017) surrounded by a persistent radio counterpart (Chatterjee et al. 2017; Marcote et al. 2017). The observation of nine VLA bursts from FRB 121102 showed that the spectra of FRB 121102 are narrow, which are characterized by a ~ 3 GHz peak frequency width of roughly ~ 500 MHz (Law et al. 2017).

Since the coherent curvature radiation by bunches always emits a wide intrinsic spectrum, e.g., $\Delta \nu / \nu \sim 1$, the observed narrow spectra might result from the absorption of low-frequency radio emission. As discussed in Section 5, at high frequencies, e.g. $\nu \gtrsim \max(\nu_{c1}, \nu_l, \nu_{\varphi})$, the spectral index is approximately $-(2p+4)/3$. Thus, if $\nu_a \gtrsim \max(\nu_{c1}, \nu_l, \nu_{\varphi})$, where ν_a is the absorption frequency, the observed spectra would be narrow.

Since FRBs have a much higher brightness temperature than that of pulsar, the fluctuating net charge number in a bunch need be much larger. Given the abrupt nature of FRBs, it is not unreasonable to introduce $\mu_c = \delta n_{\text{GJ}} / n_{\text{GJ}} \sim 1$ or even larger. If one limits $\mu_c = 1$, the extremely high brightness temperature of FRBs still require a neutron star with a stronger magnetic field and a faster rotation than normal pulsars, with the emission region close to the neutron star. This conclusion is similar to Kumar et al. (2017), although the details to achieve this conclusion are somewhat different. We adopt the following typical parameters: $D = 1$ Gpc, $R = 10^6$ cm, $B_p = 10^{14}$ G, and $P = 10$ ms⁸. The model parameters are assumed as: $L = 10$ cm, $\gamma_1 = 200$, $\rho = 3 \times 10^7$ cm, $p = 3$, $\theta = 0.1$, and $\Delta \phi = 0.1$. In this case, the distance from the emission region to the dipole field center is $r = 2.2 \times 10^6$ cm, the typical frequencies are $\nu_{c1} = 1.9$ GHz, $\nu_l = 0.9$ GHz, $\nu_{\varphi} = 1.1$ GHz, and the intrinsic maximum flux is $F_{\nu, \text{max}} = 1.6$ Jy. Due to $\nu_l < \nu_{\varphi} < \nu_{c1}$, the intrinsic spectral index α_{index} is shown in the panel (a) of Figure 12: $\alpha_{\text{index}} \sim 0.7$ for $\nu \lesssim 0.9$ GHz; $\alpha_{\text{index}} \sim -1.3$ for $0.9 \text{ GHz} \lesssim \nu \lesssim 1.1$ GHz; $\alpha_{\text{index}} \sim -2$ for $1.1 \text{ GHz} \lesssim \nu \lesssim 1.9$ GHz; $\alpha_{\text{index}} \sim -3.3$ for $\nu \gtrsim 1.9$ GHz.

Observations showed that there is a persistent radio counterpart around the repeating FRB source FRB 121102. According to Yang et al. (2016), if the FRB frequency is below the synchrotron self-absorption (SSA) frequency of the nebula, electrons in the nebula would absorb the FRB photons, leading to enhanced self-absorbed synchrotron emission, which might explain the persist radio emission of FRB 121102 (Chatterjee et al. 2017; Marcote et al. 2017; Tendulkar et al. 2017). For such

⁸ Notice that we did not invoke an even stronger magnetic field or an even shorter spin period. This is because the spindown time scale of those rapidly spinning magnetars would be shorter than the observation time of FRB 121102, which is of the order of several years.

a synchrotron nebula, its luminosity is approximately $L \simeq 4\pi r^2 [\nu_a \pi I_\nu(\nu_a)]$, where r is the nebula radius (Yang et al. 2016), where $I_\nu \simeq (2m_e/\sqrt{3}\nu_B^{1/2})\nu^{5/2}(1 - \exp(-\tau_\nu))$ is the SSA intensity, $\nu_B = eB/2\pi m_e c$ is the electron cyclotron frequency, and ν_a is the SSA frequency, which is defined by $\tau_\nu(\nu_a) = 1$. On the other hand, the FRBs with $\nu < \nu_a$ will be absorbed by the nebula, leading to a low-frequency cutoff. Thus, the synchrotron self-absorption luminosity L and the nebula magnetic field B can be constrained via (Yang et al. 2016)

$$\nu_{\text{obs}} > \nu_a \simeq 1.8 \text{ GHz} \left(\frac{B}{1 \mu\text{G}} \right)^{1/7} \times \left(\frac{L}{10^{39} \text{ erg s}^{-1}} \right)^{2/7} \left(\frac{r}{0.01 \text{ pc}} \right)^{-4/7} \quad (66)$$

and the observed peak flux is $F_{\nu, \text{obs}} \sim F_\nu(\nu_a) \simeq 0.3 \text{ Jy}$. We note that the luminosity $L \sim 10^{39} \text{ erg s}^{-1}$ is just the order of the luminosity of the persistent radio emission of FRB 121102 (Chatterjee et al. 2017; Marcote et al. 2017; Tendulkar et al. 2017). Therefore, the FRB-heated synchrotron nebulae can well explain the narrow spectrum of the bursts and the persistent radio emission.

7.2. Model B: Cosmic comb scenario

7.2.1. Curvature radiation from a combed magnetosphere

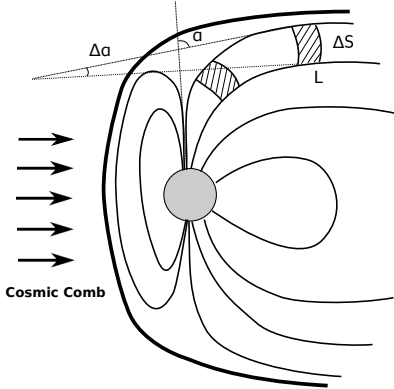


FIG. 15.— Curvature radiation from the comb magnetosphere. The shadow area denotes a bunch with length L and cross section ΔS . α denotes the angle between the magnetic axis and the magnetic field. The emission region is somewhat inside the light cylinder.

Recently, Zhang (2017) proposed that an FRB might be produced via the interaction between a nearby astrophysical plasma stream (from e.g. a nearby AGN flare, a GRB, a supernova or an outburst of a binary companion) and a foreground regular pulsar, so called “cosmic comb”. Due to the ram pressure of the stream, the magnetic field configuration of a pulsar would deviate from the dipole field configuration, meanwhile, the Goldreich-Julian outflow would be suddenly compressed following the fields, which would cause a large fluctuation of the net charge density, producing coherent bunches. When these bunches sweep across the line of sight as they are combed towards the anti-stream direction, they would make a detectable FRB. In this case, the field configuration in a bunch is similar to the Family B field lines

discussed in Section 5, and the bunch would have a larger curvature radius and a larger cross section than that in the dipole magnetosphere (see Section 5.1), since the field lines are combed to be nearly parallel to each other by the cosmic stream. Assume that the bunch opening angles are $(\Delta\phi, \Delta\alpha)$, where ϕ denotes the toroidal angle around the magnetic axis, and α denotes the angle between the magnetic axis and the magnetic field. Notice that in a combed magnetosphere, $\Delta\phi$ and $\Delta\alpha$ would be very small, since the field lines are combed to be nearly parallel to each other. The observed flux at the peak frequency ν_{peak} is given by

$$F_{\nu, \text{max}} = \frac{2\pi}{TD^2} \frac{dI}{d\omega d\Omega} \Big|_{\text{max}} \simeq \frac{2\pi e^2}{c} K(p) \frac{N_{e,0}^2 \gamma_1^4}{D^2 T} \left(\frac{\nu_{\text{peak}}}{\nu_{c1}} \right)^{2/3}. \quad (67)$$

The peak frequency is given by $\nu_{\text{peak}} = \min(\nu_l, \nu_\varphi, \nu_{c1})$, where

$$\nu_l = \frac{c}{\pi L}, \quad \nu_\varphi = \frac{3c}{2\pi\rho\varphi^3}, \quad \nu_{c1} = \frac{3c\gamma_1^3}{4\pi\rho}, \quad (68)$$

where $\varphi = \max(\Delta\alpha/2, \Delta\phi/2)$ is defined in Family B.

For a violent combing effect, within the short period of time of interest, the original Goldreich-Julian charge flow density would not be directly relevant, since the field line configuration is abruptly modified. For easy description, we relate the net charge density of a bunch with the compressed Goldreich-Julian density, i.e. $n_{\text{bun}} = (1 + \mu_c)n'_{\text{GJ}}$, where n'_{GJ} is the compressed Goldreich-Julian density, and $\mu_c n'_{\text{GJ}}$ denotes the fluctuation of the net charge density of a bunch, which contributes to the coherent radiation. Similar to Section 6.2, we define the effective electron number as $N_{e, \text{eff}}$, which corresponds to the fluctuating net charge number in a bunch. For a power-law distribution of the effective electron number, e.g., $N_e = N_{e,0}(\gamma/\gamma_1)^{-p}$ with $N_{e, \text{eff}} = \int N_e d\gamma$, the effective electron number in the compressed volume V' of a bunch is given by

$$N_{e, \text{eff}} = \gamma_1 N_{e,0}/(p-1) = \mu_c n'_{\text{GJ}} V'. \quad (69)$$

As shown in Figure 15, somewhat inside the light cylinder, the field lines are compressed by the stream, thus the net electron number density of a bunch is of the order of that at the light cylinder with a compression factor $\xi_c > 1$, e.g., $n'_{\text{GJ}} \sim \xi_c n_{\text{GJ}}(R_{\text{LC}})$. Consider that the field lines are combed to parallel to each other, the cross section of a bunch may be taken as ηR_{LC}^2 , where η is a parameter describing the cross section. One has $n'_{\text{GJ}} V' \sim \xi_c n_{\text{GJ}}(R_{\text{LC}})(\eta R_{\text{LC}}^2 L)$. Thus, the normalization of the effective electron distribution is given by

$$N_{e,0} = (p-1)\gamma_1^{-1} \mu_c n'_{\text{GJ}} V' = \frac{(p-1)\mu_c \xi_c \eta \Omega^2 B_p R^3 L}{2\pi e c^2 \gamma_1}. \quad (70)$$

Since the emission is somewhat inside the light cylinder (e.g. Zhang 2017), we approximately take the curvature radius as $\rho \sim R_{\text{LC}}$. Still assuming that the time interval between each bunch is $T \sim L/c$, one can write the peak

flux as

$$F_{\nu, \max} = \frac{(p-1)^2 K(p)}{2\pi c^4} \frac{\mu_c^2 \xi_c^2 \eta^2 \Omega^4 B_p^2 R^6 L \gamma_1^2}{D^2} \left(\frac{\nu_{\text{peak}}}{\nu_{c1}} \right)^{2/3}, \quad (71)$$

where

$$\frac{\nu_{\text{peak}}}{\nu_{c1}} = \min \left(\frac{4c}{3\Omega L \gamma_1^3}, \frac{2}{\varphi^3 \gamma_1^3}, 1 \right). \quad (72)$$

There are three cases for the peak flux: Case I: for $\nu_{\text{peak}} = \nu_l$, one has

$$F_{\nu, \max} = \frac{(p-1)^2 K(p)}{2\pi c^{10/3}} \left(\frac{4}{3} \right)^{2/3} \frac{\mu_c^2 \xi_c^2 \eta^2 \Omega^{10/3} B_p^2 R^6 L^{1/3}}{D^2}. \quad (73)$$

Case II: for $\nu_{\text{peak}} = \nu_\varphi$, one has

$$F_{\nu, \max} = \frac{(p-1)^2 K(p)}{2^{1/3} \pi c^4} \frac{\mu_c^2 \xi_c^2 \eta^2 \Omega^4 B_p^2 R^6 L}{D^2 \varphi^2}. \quad (74)$$

Case III: for $\nu_{\text{peak}} = \nu_{c1}$, one has

$$F_{\nu, \max} = \frac{(p-1)^2 K(p)}{2\pi c^4} \frac{\mu_c^2 \xi_c^2 \eta^2 \Omega^4 B_p^2 R^6 L \gamma_1^2}{D^2}. \quad (75)$$

7.2.2. Model confronted with the FRB data

Let us take a conservative approach⁹ by adopting $\mu_c = 1$ and $\xi_c = 10$. For the cosmic comb model for FRBs (Zhang 2017), we adopt the following typical parameters: $D = 1$ Gpc, $R = 10^6$ cm, $B_p = 10^{13}$ G, and $P = 0.1$ s. The model parameter is assumed to be: $L = 10$ cm, $\gamma_1 = 600$, $\rho = c/\Omega = 4.8 \times 10^8$ cm, $p = 3$, $\eta = 0.1$, and $\varphi = \max(\Delta\alpha/2, \Delta\phi/2) = 0.003$. In this case, the typical frequencies are $\nu_{c1} = 3.2$ GHz, $\nu_l = 0.9$ GHz, $\nu_\varphi = 1.1$ GHz, and the intrinsic maximum flux is $F_{\nu, \max} = 2.3$ Jy. Due to $\nu_l < \nu_\varphi < \nu_{c1}$, the predicted spectral index α_{index} is shown in the panel (a) of Figure 12: $\alpha_{\text{index}} \sim 0.7$ for $\nu \lesssim 0.9$ GHz; $\alpha_{\text{index}} \sim -1.3$ for $0.9 \text{ GHz} \lesssim \nu \lesssim 1.1$ GHz; $\alpha_{\text{index}} \sim -2$ for $1.1 \text{ GHz} \lesssim \nu \lesssim 3.2$ GHz; $\alpha_{\text{index}} \sim -3.3$ for $\nu \gtrsim 3.2$ GHz.

In the cosmic comb model, the ram pressure P_r should exceed the magnetic pressure P_B at the light cylinder $R_{\text{LC}} = c/\Omega \simeq 4.8 \times 10^8 \text{ cm}(P/0.1 \text{ s})$ (Zhang 2017). In the above parameter, the magnetic pressure at R_{LC} is

$$P_B \simeq \frac{B_p^2}{8\pi} \left(\frac{\Omega R}{c} \right)^6 \simeq 3.4 \times 10^8 \text{ erg cm}^{-3} \left(\frac{B_p}{10^{13} \text{ G}} \right)^2 \left(\frac{P}{0.1 \text{ s}} \right)^{-6} \quad (76)$$

And the ram pressure of the continuous wind from the companion star R_{LC} is

$$P_s \simeq \frac{\dot{M} v}{4\pi r^2} \simeq 3.4 \times 10^8 \text{ erg cm}^{-3} \left(\frac{\dot{M}}{M_\odot \text{ yr}^{-1}} \right) \left(\frac{\beta}{0.5} \right) \left(\frac{r}{\text{AU}} \right)^{-2} \quad (77)$$

⁹ In principle, the fluctuation parameter μ_c could exceed unity given the abruptness of the combing event, and the compression parameter ξ_c should be at least a few times greater than unity.

where \dot{M} is the wind mass-loss rate, r is the distance from the source that produce the stream, e.g. a putative companion star, and $v = \beta c$ is the wind velocity. Thus, the adopt parameters satisfy the condition for a cosmic comb.

At last, in order to explain the narrow spectrum of FRB 121102, we also consider the synchrotron self-absorption from the FRB-heated synchrotron nebula (Yang et al. 2016), as discussed in Section 7.1. Thus, the observed peak flux is $F_{\nu, \text{obs}} \sim F_\nu(\nu_a) \simeq 0.3$ Jy. This scenario also requires that the combed pulsar is within the nebula (not necessarily at the center). As shown in Eq.(66), the radius of the nebula is larger than the separation between the combing source and the combed pulsar, consistent with our expectation.

8. CONCLUSIONS AND DISCUSSIONS

In this work, we developed a general radiation theory of coherent curvature radiation by bunches under three-dimensional magnetic field geometry from the first principles. The most intriguing finding of our theory is that coherent emission in a pulsar magnetosphere is generated by the fluctuation of the net charges. With the “bunches” whose net charge density slightly deviated from the Goldreich-Julian density (e.g. $\mu_c = \delta n_{\text{GJ}}/n_{\text{GJ}} = 0.1$), the observed high brightness temperature of radio pulsars can be reproduced. Such a picture is different from the traditional pulsar models, which invokes secondary electron-positron pairs created from the inner gap near the stellar surface to produce radio emission (Sturrock 1971; Ruderman & Sutherland 1975; Zhang & Harding 2000). Even though the total lepton number density, n_\pm , in the magnetosphere is greatly increased with respect to the Goldreich-Julian density, n_{GJ} , in a pair-dominated magnetosphere, i.e. $n_\pm \sim \mathcal{M} n_{\text{GJ}}$, where $\mathcal{M} \gg 1$ is the multiplicity of the electron-positron pair cascade, the net charge density remains close to the Goldreich-Julian, and the radiation of the pairs would essentially cancel out if they are spatially bunched together. Observationally, pulsars that emit radio emission seems to follow the condition of pair production (Ruderman & Sutherland 1975; Zhang & Harding 2000). The connection between coherent radiation and pair production might be indirect. For example, violent pair production and their spatial separation (in order to “screen” process to the parallel electric field in the gap region) would induce deviations of the local net charge densities from the Goldreich-Julian density to produce coherent radiation. Notice that in some recent works on coherent curvature radiation by bunches for FRBs (e.g. Kumar et al. 2017; Lu & Kumar 2017), bunches of electron-positron pairs have been considered to produce coherent curvature radiation. The coherent radiation energy would be overestimated in these investigations.

Since the observed duration of one pulse from pulsars or FRBs, $T_{\text{obs}} \gtrsim 1$ ms, is much longer than the pulse duration of the curvature radiation, $T_p \sim 1/\nu_{\text{obs}} \sim 1$ ns, there must be many bunches sweeping cross the line of sight during the observed duration. On the other hand, due to the velocity spread and Coulomb repulsion, the bunches would be dispersed. For the velocity spread, the linear extent of the bunch is $\Delta l_v \sim \Delta v t \sim ct/\gamma^2 \sim 30 \text{ cm}(t/1 \text{ ms})(\gamma/10^3)^{-2}$. For Coulomb repulsion, according to Cheng & Ruderman (1977), the

linear extent caused by the velocity difference between electron and positron is $\Delta l_c \sim |v_+ - v_-|t \sim ct/\mathcal{M} \sim 30 \text{ cm}(t/0.01 \text{ ms})(\mathcal{M}/10^4)^{-1}$, where v_+ and v_- are the velocities of electrons and positrons, respectively. Therefore, for GHz wave, the dispersion time, T_d , of a bunch may be solved by $\lambda \sim \max(\Delta l_v(T_d), \Delta l_c(T_d))$, leading to $T_d \sim 0.01 \text{ ms}$ for $\gamma \sim 10^3$ and $\mathcal{M} \sim 10^4$. In fact, the existence of many bunches during the observational time suggests that bunches are continuously generated. As long as the bunch generation time scale is shorter than the dispersion time scale, bunches can be maintained to power the observed coherent emission. This would be possible for an unstable polar cap region as invoked in most pulsar models (e.g. Ruderman & Sutherland 1975; Egorenkov et al. 1983; Zhang et al. 1997; Gil & Sendyk 2000; Gil et al. 2006; Gedalin et al. 2002; Levinson et al. 2005; Beloborodov & Thompson 2007; Luo & Melrose 2008; Kumar et al. 2017; Lu & Kumar 2017).

Another interesting finding of our paper is that with the three-dimensional magnetic field configuration considered, one can quantify the coherent curvature radiation of the bunches for the first time. We consider that a bunch, consisting of a trajectory family, is characterized by the following parameters: bunch length L , curvature radius ρ of the trajectory family, bunch opening angles $(\varphi_\times, \varphi_+)$, and electron energy distribution $N_e(\gamma)d\gamma$ with $\gamma_1 < \gamma < \gamma_2$. The radiation spectrum shows a multi-segment broken power law with the break frequencies $\nu_{c1} = 3c\gamma_1^3/4\pi\rho$, $\nu_l = c/\pi L$, and $\nu_\phi = 3c/2\pi\rho\varphi^3$ where φ depends on $(\varphi_\times, \varphi_+)$ and the field configuration in the bunch. The spectral indices depend on the relative order of these characteristic frequencies. The detailed spectra are presented in Section 5.1 and Section 5.2.

The coherent mechanism of pulsar radio emission has been subject to debate over the years (Melrose 2017). Our study suggests that coherent curvature radiation by bunches remains a promising candidate to interpret the observations. In particular, the observed spectra of pulsars, which can be fitted by either a single power law, or two-segment or multi-segment broken power laws (e.g. Lorimer et al. 1995; Xilouris et al. 1996; Jankowski et al. 2017), can be naturally interpreted with our model given typical pulsar parameters (e.g. $B_p = 10^{12} \text{ G}$ and $P = 0.1 \text{ s}$). The required fluctuation is only moderate (e.g. $\mu_c = \delta n_{\text{GJ}}/n_{\text{GJ}} \sim 0.1$).

The physical origin of FRBs is mysterious. Many FRB models invoked coherent curvature radiation by bunches to explain their extremely brightness temperature, e.g., pulsar-like activities (Connor et al. 2016; Cordes & Wasserman 2016; Metzger et al. 2017a; Kashiyama & Murase 2017), mergers of compact binaries (Kashiyama et al. 2013; Totani 2013; Wang et al. 2016; Zhang 2016; Liu et al. 2016), collapse of supramassive neutron stars to black holes (Falcke & Rezzolla 2014; Zhang 2014), collisions between pulsars and a comet or asteroids (Geng & Huang 2015; Dai et al. 2016), cosmic combs (Zhang 2017), and so on. However, most FRB models mainly focused on the release energy and duration, with the description of coherent radiation overly simplified. For FRBs, due to their extremely high brightness temperature, the fluctuating net charge density of a bunch should be much greater than that of pulsars. Several factors may contribute to such a large fluctuating net charges:

1. The FRB source may involve a neutron star with a stronger magnetic field and faster rotation (e.g. Murase et al. 2016; Metzger et al. 2017b) with the emission region close to the stellar surface (e.g. Kumar et al. 2017).
2. Due to the abrupt nature of FRBs, the normalized fluctuation of the net charge density μ_c for FRBs may reach or even exceed unity.
3. In the cosmic comb scenario (Zhang 2017), the magnetosphere may be suddenly compressed by an astrophysical stream so that the effective fluctuation μ_c should exceed unity. Meanwhile, since the field lines are combed to nearly parallel to each other, the cross section of a bunch could be very large, leading to more significant coherent emission. The bunching coherent mechanism proposed in this paper can interpret the steep negative spectral index observed in the bursts detected from the repeating source FRB 121102. In order to account for the narrowness of the spectrum, one needs to introduce synchrotron self-absorption from the FRB-heated synchrotron nebula (Yang et al. 2016). The required nebula luminosity of this model coincides with the observed luminosity of the persistent radio emission of FRB 121102 (Chatterjee et al. 2017).

In the above discussion, we have assumed that the emission region of the curvature radiation is in the open field lines rather than the closed field lines. The main reason is that bunches from the open field line region would move along the field lines that curve away from the emitted coherent radio waves, so that they are not subject to further absorption by the proceeding bunches. Emission from the bunches moving in closed field line regions may be subject to further absorption by bunches moving along adjacent field lines. The radiation in these cases would not be narrowly beamed, which might give rise to smoother lightcurves than observed. Pulsar radio emission is known to originate from the open field line regions of pulsars (e.g. Rankin 1983). For FRBs, models that invoke open field lines are favored. Those invoking closed field lines require further justification regarding the propagation of the coherent radio waves across the magnetosphere of the source.

Finally, we'd like to comment that some basic conditions of the classical formula, e.g., Eq.(4) and Eq.(12), have been omitted in some previous works when applied to study curvature radiation (e.g. Ghisellini & Locatelli 2017). Below are some examples: 1. Equation (12) was often used to describe the spectrum of curvature radiation. However, one should note that the classical $\nu^{1/3}$ spectrum corresponds to the total radiation spectrum in all directions rather than the direction along the line of sight (e.g. Jackson 1998; Rybicki & Lightman 1979). For curvature radiation, the radiation of one bunch is beamed in a narrow cone that sweeps across the line of sight, thus one should consider the radiation per unit solid angle, rather than the total radiation spectrum. Even considering more than one bunch with different motion directions, a coherent sum of amplitudes should be considered, rather than the simple integration over angles. This leads to the $\nu^{2/3}$ spectrum presented in this paper. 2. The definition of radiation power should be based on the average time scale, T , of pulse repetition, as shown in Eq.(4). For synchrotron radiation, pulses repeat naturally with the gyration period. However, for one-time

curvature radiation, the average time scale of pulse repetition depends on the average time interval between the bunches, instead of the gyration period. 3. Since the basic formulae about the radiation of moving charges, e.g., Eq.(3), can be applied to relativistic charged particles, it is unnecessary to repeatedly apply some relativistic effects, such as time delay, beaming effect and so on, to

the derive $dI/d\omega d\Omega$, etc. (cf. Eq.(3)).

This work is partially supported by Project funded by the Initiative Postdocs Supporting Program (No. BX201600003), the National Basic Research Program (973 Program) of China (No. 2014CB845800), and the China Postdoctoral Science Foundation (No. 2016M600851). Y.-P.Y. is supported by a KIAA-CAS Fellowship.

REFERENCES

- Beloborodov, A. M. 2017, *ApJ*, 843, L26
 Beloborodov, A. M., & Thompson, C. 2007, *ApJ*, 657, 967
 Benford, G., & Buschauer, R. 1977, *MNRAS*, 179, 189
 Blandford, R. D. 1975, *MNRAS*, 170, 551
 Buschauer, R., & Benford, G. 1976, *MNRAS*, 177, 109
 Chatterjee, S., Law, C. J., Wharton, R. S., et al. 2017, *ArXiv e-prints*, arXiv:1701.01098
 Cheng, A. F., & Ruderman, M. A. 1977, *ApJ*, 212, 800
 Cocke, W. J. 1973, *ApJ*, 184, 291
 Connor, L., Sievers, J., & Pen, U.-L. 2016, *MNRAS*, 458, L19
 Cordes, J. M., & Wasserman, I. 2016, *MNRAS*, 457, 232
 Dai, Z. G., Wang, J. S., Wu, X. F., & Huang, Y. F. 2016, *ApJ*, 829, 27
 Egorenkov, V. D., Lominadze, D. G., & Mamradze, P. G. 1983, *Astrophysics*, 19, 426
 Falcke, H., & Rezzolla, L. 2014, *A&A*, 562, A137
 Gedalin, M., Gruman, E., & Melrose, D. B. 2002, *MNRAS*, 337, 422
 Geng, J. J., & Huang, Y. F. 2015, *ApJ*, 809, 24
 Ghisellini, G. 2017, *MNRAS*, arXiv:1609.04815
 Ghisellini, G., & Locatelli, N. 2017, *ArXiv e-prints*, arXiv:1708.07507
 Gil, J., Lyubarsky, Y., & Melikidze, G. I. 2004, *ApJ*, 600, 872
 Gil, J., Melikidze, G., & Zhang, B. 2006, *ApJ*, 650, 1048
 Gil, J. A., & Sendyk, M. 2000, *ApJ*, 541, 351
 Ginzburg, V. L., & Zhelezniakov, V. V. 1975, *ARA&A*, 13, 511
 Goldreich, P., & Julian, W. H. 1969, *ApJ*, 157, 869
 Gunn, J. E., & Ostriker, J. P. 1971, *ApJ*, 165, 523
 Hankins, T. H., & Eilek, J. A. 2007, *ApJ*, 670, 693
 Jackson, J. D. 1998, *Classical Electrodynamics*, 3rd Edition (New York: Wiley), 832
 Jankowski, F., van Straten, W., Keane, E. F., et al. 2017, *ArXiv e-prints*, arXiv:1709.08864
 Kashiwama, K., Ioka, K., & Mészáros, P. 2013, *ApJ*, 776, L39
 Kashiwama, K., & Murase, K. 2017, *ApJ*, 839, L3
 Katz, J. I. 2014, *Phys. Rev. D*, 89, 103009
 Kazbegi, A. Z., Machabeli, G. Z., & Melikidze, G. I. 1991, *MNRAS*, 253, 377
 Kellermann, K. I., & Pauliny-Toth, I. I. K. 1969, *ApJ*, 155, L71
 Kroll, N. M., & McMullin, W. A. 1979, *ApJ*, 231, 425
 Kumar, P., Lu, W., & Bhattacharya, M. 2017, *MNRAS*, 468, 2726
 Law, C. J., Abruzzo, M. W., Bassa, C. G., et al. 2017, *ApJ*, 850, 76
 Levinson, A., Melrose, D., Judge, A., & Luo, Q. 2005, *ApJ*, 631, 456
 Liu, T., Romero, G. E., Liu, M.-L., & Li, A. 2016, *ApJ*, 826, 82
 Lorimer, D. R., Bailes, M., McLaughlin, M. A., Narkevic, D. J., & Crawford, F. 2007, *Science*, 318, 777
 Lorimer, D. R., Yates, J. A., Lyne, A. G., & Gould, D. M. 1995, *MNRAS*, 273, 411
 Lu, W., & Kumar, P. 2017, *ArXiv e-prints*, arXiv:1710.10270
 Luo, Q., & Melrose, D. 2008, *MNRAS*, 387, 1291
 Luo, Q., & Melrose, D. B. 1992, *MNRAS*, 258, 616
 —. 1995, *MNRAS*, 276, 372
 Lyubarsky, Y. 2014, *MNRAS*, 442, L9
 Lyutikov, M., Blandford, R. D., & Machabeli, G. 1999a, *MNRAS*, 305, 338
 Lyutikov, M., Machabeli, G., & Blandford, R. 1999b, *ApJ*, 512, 804
 Machabeli, G. Z., & Usov, V. V. 1979, *Soviet Astronomy Letters*, 5, 445
 Marcote, B., Paragi, Z., Hessels, J. W. T., et al. 2017, *ApJ*, 834, L8
 McCray, R. 1966, *Science*, 154, 1320
 Melrose, D. B. 1978, *ApJ*, 225, 557
 —. 2017, *ArXiv e-prints*, arXiv:1707.02009
 Melrose, D. B., & Gedalin, M. E. 1999, *ApJ*, 521, 351
 Metzger, B. D., Berger, E., & Margalit, B. 2017a, *ApJ*, 841, 14
 —. 2017b, *ApJ*, 841, 14
 Murase, K., Kashiwama, K., & Mészáros, P. 2016, *MNRAS*, 461, 1498
 Rankin, J. M. 1983, *ApJ*, 274, 333
 Ruderman, M. A., & Sutherland, P. G. 1975, *ApJ*, 196, 51
 Rybicki, G. B., & Lightman, A. P. 1979, *Radiative processes in astrophysics* (New York: Wiley-Interscience)
 Sturrock, P. A. 1971, *ApJ*, 164, 529
 Tendulkar, S. P., Bassa, C. G., Cordes, J. M., et al. 2017, *ApJ*, 834, L7
 Thornton, D., Stappers, B., Bailes, M., et al. 2013, *Science*, 341, 53
 Totani, T. 2013, *PASJ*, 65, L12
 Twiss, R. Q. 1958, *Australian Journal of Physics*, 11, 564
 Wang, J.-S., Yang, Y.-P., Wu, X.-F., Dai, Z.-G., & Wang, F.-Y. 2016, *ApJ*, 822, L7
 Waxman, E. 2017, *ApJ*, 842, 34
 Weatherall, J. C. 1998, *ApJ*, 506, 341
 Xilouris, K. M., Kramer, M., Jessner, A., Wielebinski, R., & Timofeev, M. 1996, *A&A*, 309, 481
 Yang, Y.-P., Zhang, B., & Dai, Z.-G. 2016, *ApJ*, 819, L12
 Zhang, B. 2014, *ApJ*, 780, L21
 —. 2016, *ApJ*, 827, L31
 —. 2017, *ApJ*, 836, L32
 Zhang, B., & Harding, A. K. 2000, *ApJ*, 532, 1150
 Zhang, B., & Qiao, G. J. 1996, *A&A*, 310, 135
 Zhang, B., Qiao, G. J., Lin, W. P., & Han, J. L. 1997, *ApJ*, 478, 313
 Zhelezniakov, V. V., & Shaposhnikov, V. E. 1979, *Australian Journal of Physics*, 32, 49

APPENDIX

A. RADIATION FROM A SINGLE MOVING CHARGE

Based on the time-dependent electromagnetic field of a single moving charge (see Eq.(1)), the radiation frequency spectrum can be calculated by the Fourier transformation. First, the power radiated per unit solid angle has a general form, e.g.,

$$\frac{dP(t)}{d\Omega} = |\mathbf{A}(t)|^2, \quad \text{where} \quad \mathbf{A}(t) \equiv \left(\frac{c}{4\pi}\right)^{1/2} [\mathbf{RE}]_{\text{ret}}, \quad (\text{A1})$$

and t is the observed time at the field point, R is the distance between the field point and the retarded position of the moving charge. The observed point is assumed to be far enough away from the source. We introduce Fourier and its inverse transformations, e.g.,

$$\mathbf{A}(\omega) = \frac{1}{\sqrt{2\pi}} \int_{-\infty}^{+\infty} \mathbf{A}(t) e^{i\omega t} dt, \quad \mathbf{A}(t) = \frac{1}{\sqrt{2\pi}} \int_{-\infty}^{+\infty} \mathbf{A}(\omega) e^{-i\omega t} d\omega. \quad (\text{A2})$$

Since acceleration-field term in Eq.(1) falls off as $1/R$, it dominates in the “far zone”. Using Eq.(1) and Eq.(A2) and changing variables from the observed time t to the retarded time t' , one has

$$\mathbf{A}(\omega) = \left(\frac{e^2}{8\pi^2 c} \right)^{1/2} (-i\omega) \int_{-\infty}^{+\infty} \mathbf{n} \times (\mathbf{n} \times \boldsymbol{\beta}) e^{i\omega(t' - \mathbf{n} \cdot \mathbf{r}(t')/c)} dt', \quad (\text{A3})$$

where $\mathbf{r}(t')$ denotes the retarded position of the moving charge, $\boldsymbol{\beta}$ and \mathbf{n} are defined as $\boldsymbol{\beta} = \dot{\mathbf{r}}(t')/c$ and $\mathbf{n} = \mathbf{R}/R$. Here \mathbf{R} is defined as $\mathbf{R} = \mathbf{x} - \mathbf{r}(t')$ and \mathbf{x} is the field point. For $r(t') \ll x$, one has $R(t') \simeq x - \mathbf{n} \cdot \mathbf{r}(t')$, which has been considered in the above integral. Note that in Eq.(A3), we have used the identity $\mathbf{n} \times [(\mathbf{n} - \boldsymbol{\beta}) \times \dot{\boldsymbol{\beta}}] / (1 - \mathbf{n} \cdot \boldsymbol{\beta})^2 = d/dt [\mathbf{n} \times (\mathbf{n} \times \boldsymbol{\beta}) / (1 - \mathbf{n} \cdot \boldsymbol{\beta})]$. The total energy radiated per unit solid angle is given by (Jackson 1998)

$$\begin{aligned} \frac{dW}{d\Omega} &= \int_{-\infty}^{+\infty} \frac{dP(t)}{d\Omega} dt = \int_0^{+\infty} \frac{dI(\omega, \mathbf{n})}{d\omega d\Omega} d\omega \\ &= \int_{-\infty}^{+\infty} |\mathbf{A}(t)|^2 dt = \int_{-\infty}^{+\infty} |\mathbf{A}(\omega)|^2 d\omega, \end{aligned} \quad (\text{A4})$$

where $dI/d\omega d\Omega$ denotes the energy radiated per unit solid angle per unit frequency interval. Due to $dI/d\omega d\Omega = 2|\mathbf{A}(\omega)|^2$, one has (e.g. Jackson 1998; Rybicki & Lightman 1979)

$$\frac{dI}{d\omega d\Omega} = \frac{e^2 \omega^2}{4\pi^2 c} \left| \int_{-\infty}^{+\infty} \mathbf{n} \times (\mathbf{n} \times \boldsymbol{\beta}) e^{i\omega(t - \mathbf{n} \cdot \mathbf{r}(t)/c)} dt \right|^2. \quad (\text{A5})$$

For brevity, the primes on the time variable have been omitted.

B. RADIATION FROM A POINT SOURCE WITH POWER-LAW DISTRIBUTED ELECTRONS

We consider that the radiation from a point containing relativistic electrons with different energies. The energy distribution of the electrons is assumed to be a power-law distribution, e.g.

$$N_e(\gamma) = N_{e,0} \left(\frac{\gamma}{\gamma_1} \right)^{-p}, \quad \gamma_1 < \gamma < \gamma_2 \quad (\text{B1})$$

where $N_e(\gamma)d\gamma$ is the electron number in a range from γ to $\gamma + d\gamma$, $N_{e,0}$ is the corresponding normalization, γ_1 and γ_2 are the lower and upper limits of Lorentz factor. The energy radiated per unit frequency interval per unit solid angle is given by

$$\frac{dI}{d\omega d\Omega} = \frac{e^2 \omega^2}{4\pi^2 c} \left| -\epsilon_{\parallel} \int_{\gamma_1}^{\gamma_2} N_e(\gamma) A_{\parallel}(\omega, \gamma) d\gamma + \epsilon_{\perp} \int_{\gamma_1}^{\gamma_2} N_e(\gamma) A_{\perp}(\omega, \gamma) d\gamma \right|^2. \quad (\text{B2})$$

If the observed direction is in the trajectory plane, e.g., $\theta = 0$, the perpendicular polarized component is zero, e.g., $A_{\perp}(\omega, \gamma) = 0$. Thus, one has

$$\frac{dI}{d\omega d\Omega} = \frac{e^2 \omega^2}{4\pi^2 c} \left| \int_{\gamma_1}^{\gamma_2} N_e(\gamma) A_{\parallel}(\omega, \gamma) d\gamma \right|^2, \quad (\text{B3})$$

where the parallel polarized amplitude is given by Eq.(6), e.g.,

$$A_{\parallel}(\omega, \gamma) = \frac{2i}{\sqrt{3}} \frac{\rho}{c\gamma^2} K_{2/3} \left(\frac{\omega\rho}{3c\gamma^3} \right) \simeq \frac{2^{4/3}i}{\sqrt{3}} \Gamma(2/3) \frac{\rho}{c\gamma^2} \left(\frac{\omega}{\omega_c} \right)^{-2/3} e^{-\omega/2\omega_c}. \quad (\text{B4})$$

Here, we use the approximation $K_{\nu}(x) \sim (\Gamma(\nu)/2)(x/2)^{-\nu} e^{-x}$. The coherent sum of the amplitudes is given by

$$\int_{\gamma_1}^{\gamma_2} N_e(\gamma) A_{\parallel}(\omega, \gamma) d\gamma = \frac{2^{4/3}i}{3^{3/2}} \Gamma(2/3) N_{e,0} \frac{\rho}{c\gamma_1} \left(\frac{\omega}{\omega_{c1}} \right)^{-(p+1)/3} \int_{x_2}^{x_1} x^{(p-4)/3} e^{-x/2} dx, \quad (\text{B5})$$

where $x_1 = \omega/\omega_{c1}$, $x_2 = \omega/\omega_{c2}$, $x = \omega/\omega_c$, $\omega_{c1} = \omega_c(\gamma_1)$, and $\omega_{c2} = \omega_c(\gamma_2)$. The radiation energy satisfies

$$\frac{dI}{d\omega d\Omega} \simeq \frac{e^2}{c} \left[\frac{\Gamma(2/3)}{\pi} \right]^2 \frac{1}{3 \cdot 2^{4/3}} N_{e,0}^2 \gamma_1^4 \left(\frac{\omega}{\omega_{c1}} \right)^{-(2p-4)/3} \left(\int_{x_2}^{x_1} x^{(p-4)/3} e^{-x/2} dx \right)^2. \quad (\text{B6})$$

If $x_2 \ll 1$ and $x_2 \ll x_1$, according to the property of Gamma function, one has

$$\int_{x_2}^{x_1} x^{(p-4)/3} e^{-x/2} dx = 2^{(p-1)/3} \left[\Gamma\left(\frac{p-1}{3}\right) - \Gamma\left(\frac{p-1}{3}, \frac{x_1}{2}\right) \right]. \quad (\text{B7})$$

If $x_1 \rightarrow \infty$, $\Gamma((p-1)/3, x_1/2) \rightarrow 0$, for the power-law distribution of electrons, the energy radiated per unit frequency interval per unit solid angle is given by

$$\frac{dI}{d\omega d\Omega} \simeq \frac{e^2}{c} \frac{2^{(2p-6)/3}}{3\pi^2} \left[\Gamma\left(\frac{2}{3}\right) \Gamma\left(\frac{p-1}{3}\right) \right]^2 N_{e,0}^2 \gamma_1^4 \begin{cases} \left(\frac{\omega}{\omega_{c1}}\right)^{2/3}, & \omega \ll \omega_{c1}, \\ \left(\frac{\omega}{\omega_{c1}}\right)^{-(2p-4)/3} e^{-\omega/\omega_{c2}}, & \omega \gg \omega_{c1}. \end{cases} \quad (\text{B8})$$

C. TRAJECTORY FAMILY II: GENERATED VIA ROTATION AROUND Y AXIS

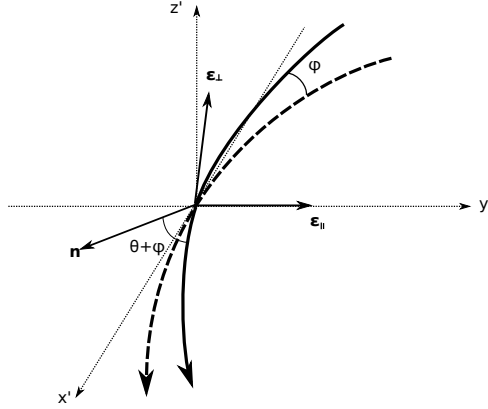


FIG. 16.— Geometry for instantaneously circular motion for Family II in the local frame. The dashed line denotes the trajectory lies in the $x' - y'$ plane. At retarded time $t = 0$, the electron is at the origin, and the velocity is along x' axis. The solid line denotes a trajectory generated via the rotation around y' axis by the dashed line (corresponding to a trajectory generated via the rotation around y axis in Figure 6 when \mathbf{n} is parallel to the x' axis.).

In this section, we consider that the trajectory family is generated via the rotation around y axis in Figure 6. In the local frame, as shown in Figure 16, the amplitude of one in the trajectory family can be calculated following Section 3.1, with the observation angle θ replaced by $\theta + \varphi_j$, where φ_j corresponds to the angle between the j th trajectory and the median trajectory. The energy radiated per unit frequency interval per unit solid angle is given by

$$\frac{dI}{d\omega d\Omega} = \frac{e^2 \omega^2}{4\pi^2 c} \left| -\epsilon_{\parallel} \sum_j^N A_{\parallel,j}(\omega) + \epsilon_{\perp} \sum_j^N A_{\perp,j}(\omega) \right|^2 \quad (\text{C1})$$

First, we assume that the bunch opening angle of the N trajectories is 2φ , each trajectory is uniformly spaced in the bunch opening angle, and there is only one electron in each trajectory. Then the amplitudes in the above equation are given by

$$\begin{aligned} \sum_j^N A_{\parallel,j}(\omega) &= \frac{N}{2\varphi} \int_{-\varphi}^{\varphi} \frac{\rho}{c} \left[\frac{1}{\gamma^2} + (\theta + \varphi')^2 \right] \frac{2i}{\sqrt{3}} K_{2/3}(\xi) d\varphi' \\ \sum_j^N A_{\perp,j}(\omega) &= \frac{N}{2\varphi} \int_{-\varphi}^{\varphi} \frac{\rho(\theta + \varphi')}{c} \left[\frac{1}{\gamma^2} + (\theta + \varphi')^2 \right]^{1/2} \frac{2}{\sqrt{3}} K_{1/3}(\xi) d\varphi', \end{aligned} \quad (\text{C2})$$

where

$$\xi = \frac{\omega \rho}{3c} \left[\frac{1}{\gamma^2} + (\theta + \varphi')^2 \right]^{3/2}. \quad (\text{C3})$$

Since the radiation is beamed in a narrow cone that sweeps cross the observation point, we are only interested in the

case with $\theta = 0$. One has

$$\begin{aligned} \sum_j^N A_{\parallel,j}(\omega) &= \frac{N}{2\varphi} \int_{-\varphi}^{\varphi} \frac{\rho}{c} \left(\frac{1}{\gamma^2} + \varphi'^2 \right) \frac{2i}{\sqrt{3}} K_{2/3}(\xi) d\varphi' \\ \sum_j^N A_{\perp,j}(\omega) &= 0. \end{aligned} \quad (\text{C4})$$

We define

$$\varphi_c \equiv \frac{1}{\gamma} \left(\frac{2\omega_c}{\omega} \right)^{1/3} = \left(\frac{3c}{\omega\rho} \right)^{1/3}. \quad (\text{C5})$$

For any $\varphi' \gg \varphi_c$, one has $\xi \gg 1$, leading to $K_{2/3}(\xi) \rightarrow 0$. Therefore, one has approximately

$$\sum_j^N A_{\parallel,j}(\omega) = \frac{N}{2\varphi} \int_{-\varphi}^{\varphi} \frac{\rho}{c} \left(\frac{1}{\gamma^2} + \varphi'^2 \right) \frac{2i}{\sqrt{3}} K_{2/3}(\xi) d\varphi' \simeq \frac{N}{2\varphi} \frac{\rho}{c\gamma^2} \frac{2i}{\sqrt{3}} K_{2/3} \left(\frac{\omega\rho}{3c\gamma^3} \right) (2\Delta\varphi), \quad (\text{C6})$$

where

$$\Delta\varphi = \begin{cases} \varphi, & \varphi \ll \varphi_c, \\ \varphi_c, & \varphi \gg \varphi_c. \end{cases} \quad (\text{C7})$$

For $\omega_\varphi \ll \omega_c$, the sum of the parallel amplitudes is

$$\sum_j^N A_{\parallel,j}(\omega) = \frac{2^{4/3}i}{\sqrt{3}} \Gamma(2/3) N \frac{\rho}{c\gamma^2} \begin{cases} \left(\frac{\omega}{\omega_c} \right)^{-2/3}, & \omega \ll \omega_\varphi, \\ \left(\frac{\omega_\varphi}{\omega_c} \right)^{1/3} \left(\frac{\omega}{\omega_c} \right)^{-1} e^{-\omega/2\omega_c}, & \omega \gg \omega_\varphi, \end{cases} \quad (\text{C8})$$

where

$$\omega_\varphi = \frac{3c}{\rho\varphi^3}, \quad (\text{C9})$$

which is defined as $\varphi_c(\omega_\varphi) = \varphi$. Therefore, the energy radiated per unit frequency interval per unit solid angle is given by

$$\frac{dI}{d\omega d\Omega} = \frac{e^2}{c} \frac{3}{2^{4/3}} \left[\frac{\Gamma(2/3)}{\pi} \right]^2 N^2 \gamma^2 \begin{cases} \left(\frac{\omega}{\omega_c} \right)^{2/3}, & \omega \ll \omega_\varphi, \\ \left(\frac{\omega_\varphi}{\omega_c} \right)^{2/3} e^{-\omega/\omega_c}, & \omega \gg \omega_\varphi. \end{cases} \quad (\text{C10})$$

On the other hand, for $\omega_\varphi \gg \omega_c$, the radiation from the entire bunch opening angle can be observed, as shown in Figure 7. In this case, the sum of the parallel amplitudes is given by $\sum_j^N A_{\parallel,j}(\omega) = N A_{\parallel}(\omega, \gamma)$, where $A_{\parallel}(\omega, \gamma)$ is given by Eq.(B4). Thus the radiation energy is given by Eq.(10).

Next, we further consider that there are more than one electrons in a point source in each trajectory and the electron distribution satisfies the power-law distribution, e.g. $N_e(\gamma)d\gamma = N_{e,0}(\gamma/\gamma_1)^{-p}d\gamma$ for $\gamma_1 < \gamma < \gamma_2$. In the case that $\omega_\varphi \ll \omega_{c1}$, if $\omega \ll \omega_\varphi$, since ω_φ is independent of γ , one always has $dI/d\omega d\Omega \propto \omega^{2/3}$; if $\omega \gg \omega_\varphi$, one has

$$\begin{aligned} \sum_j^N A_{\parallel,j}(\omega) &= \frac{2^{5/3}i}{\sqrt{3}} \Gamma(2/3) \frac{\rho}{c\varphi} \int_{\gamma_1}^{\gamma_2} \frac{N_e(\gamma)}{\gamma^3} \left(\frac{\omega}{\omega_c} \right)^{-1} e^{-\omega/2\omega_c} d\gamma \\ &= \frac{2^{5/3}i}{3^{3/2}} \Gamma(2/3) \frac{N_{e,0}}{\varphi} \frac{\rho}{c\gamma_1^2} \left(\frac{\omega}{\omega_{c1}} \right)^{-(p+2)/3} \int_{x_2}^{x_1} x^{(p-4)/3} e^{-x/2} dx, \end{aligned} \quad (\text{C11})$$

and the radiation energy is given by

$$\begin{aligned} \frac{dI}{d\omega d\Omega} &= \frac{e^2}{c} \left[\frac{\Gamma(2/3)}{\pi} \right]^2 \frac{1}{3 \cdot 2^{2/3}} \frac{N_{e,0}^2 \gamma_1^2}{\varphi^2} \left(\frac{\omega}{\omega_{c1}} \right)^{-(2p-2)/3} \left(\int_{x_2}^{x_1} x^{(p-4)/3} e^{-x/2} dx \right)^2 \\ &\simeq \frac{e^2}{c} \frac{2^{(2p-4)/3}}{3\pi^2} \left[\Gamma\left(\frac{2}{3}\right) \Gamma\left(\frac{p-1}{3}\right) \right]^2 \frac{N_{e,0}^2 \gamma_1^2}{\varphi^2} \begin{cases} 1, & \omega \ll \omega_{c1}, \\ \left(\frac{\omega}{\omega_{c1}} \right)^{-(2p-2)/3} e^{-\omega/\omega_{c2}}, & \omega \gg \omega_{c1}. \end{cases} \end{aligned} \quad (\text{C12})$$

Note that in the above equation, we have used Eq.(B7). In the case that $\omega_{c1} \ll \omega_\varphi$, if $\omega \ll \omega_\varphi$, the radiation energy is directly given by Eq.(16); if $\omega \gg \omega_\varphi$, similar to the calculation process of Eq.(C11) and Eq.(C12), one has $dI/d\omega d\Omega \propto \omega^{-(2p-2)/3}$.

In summary, if $\omega_\varphi \ll \omega_{c1}$, the energy radiated per unit frequency interval per unit solid angle is given by

$$\frac{dI}{d\omega d\Omega} = \frac{e^2}{c} \frac{2^{(2p-6)/3}}{3\pi^2} \left[\Gamma\left(\frac{2}{3}\right) \Gamma\left(\frac{p-1}{3}\right) \right]^2 N_{e,0}^2 \gamma_1^4 \begin{cases} \left(\frac{\omega}{\omega_{c1}} \right)^{2/3}, & \omega \ll \omega_\varphi, \\ \left(\frac{\omega_\varphi}{\omega_{c1}} \right)^{2/3}, & \omega_\varphi \ll \omega \ll \omega_{c1}, \\ \left(\frac{\omega_\varphi}{\omega_{c1}} \right)^{2/3} \left(\frac{\omega}{\omega_{c1}} \right)^{-(2p-2)/3}, & \omega \gg \omega_{c1}. \end{cases} \quad (\text{C13})$$

If $\omega_\varphi \gg \omega_{c1}$, the energy radiated per unit frequency interval per unit solid angle is given by

$$\frac{dI}{d\omega d\Omega} = \frac{e^2}{c} \frac{2^{(2p-6)/3}}{3\pi^2} \left[\Gamma\left(\frac{2}{3}\right) \Gamma\left(\frac{p-1}{3}\right) \right]^2 N_{e,0}^2 \gamma_1^4 \begin{cases} \left(\frac{\omega}{\omega_{c1}} \right)^{2/3}, & \omega \ll \omega_{c1}, \\ \left(\frac{\omega}{\omega_{c1}} \right)^{-(2p-4)/3}, & \omega_{c1} \ll \omega \ll \omega_\varphi, \\ \left(\frac{\omega_\varphi}{\omega_{c1}} \right)^{-(2p-4)/3} \left(\frac{\omega}{\omega_\varphi} \right)^{-(2p-2)/3}, & \omega \gg \omega_\varphi. \end{cases} \quad (\text{C14})$$

D. TRAJECTORY FAMILY III: GENERATED VIA ROTATION AROUND X AXIS

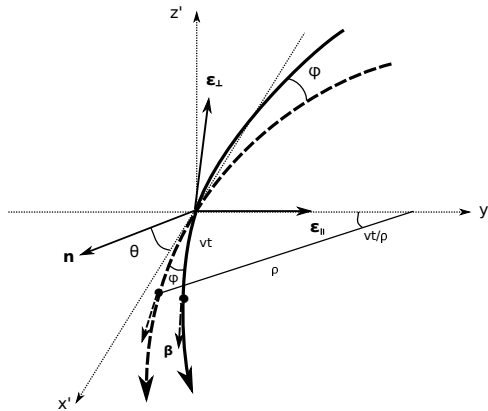


FIG. 17.— Geometry for instantaneously circular motion for Family III in the local frame. The dashed line denotes the trajectory lies in the $x' - y'$ plane. At retarded time $t = 0$, the electron is at the origin, and the velocity is along x' axis. The solid line denotes a trajectory generated via the rotation around z' axis by the dashed line (corresponding to a trajectory generated via the rotation around x axis in Figure 8 when \mathbf{n} is parallel to the x' axis.), which is also in the $x' - y'$ plane.

For the trajectory family generated via the rotation around x axis, as shown Figure 8, we need to consider a more general situation to calculate the amplitude from each trajectory than that in Section 3.1. In the local frame, as shown in Figure 17, all the trajectories are in the $x' - y'$ plane, and the angle between the electron velocity direction and x' axis at $t = 0$, is defined as φ_j , where $\varphi = 0$ corresponds to the case of Section 3.1. The vector term in the integrand

Eq.(3) can be written as

$$\mathbf{n} \times (\mathbf{n} \times \boldsymbol{\beta}_j) = \beta \left[-\boldsymbol{\epsilon}_{\parallel} \sin \left(\frac{vt}{\rho} + \varphi_j \right) + \boldsymbol{\epsilon}_{\perp} \cos \left(\frac{vt}{\rho} + \varphi_j \right) \sin \theta \right]. \quad (\text{D1})$$

The exponential term in the integrand Eq.(3) is given by

$$\begin{aligned} \omega \left(t - \frac{\mathbf{n} \cdot \mathbf{r}_j(t)}{c} \right) &= \omega \left[t - \frac{2\rho}{c} \sin \left(\frac{vt}{2\rho} \right) \cos \left(\frac{vt}{2\rho} + \varphi_j \right) \cos \theta \right] \\ &\simeq \frac{\omega}{2} \left[\left(\frac{1}{\gamma^2} + \theta^2 + \varphi_j^2 \right) t + \frac{c^2 t^3}{3\rho^2} + \frac{ct^2}{\rho} \varphi_j \right]. \end{aligned} \quad (\text{D2})$$

Therefore, the amplitudes are given by

$$A_{\parallel,j} \simeq \int_{-\infty}^{\infty} \left(\frac{ct}{\rho} + \varphi_j \right) \exp \left(i \frac{\omega}{2} \left[\left(\frac{1}{\gamma^2} + \theta^2 + \varphi_j^2 \right) t + \frac{c^2 t^3}{3\rho^2} + \frac{ct^2}{\rho} \varphi_j \right] \right) dt, \quad (\text{D3})$$

$$A_{\perp,j} \simeq \theta \int_{-\infty}^{\infty} \exp \left(i \frac{\omega}{2} \left[\left(\frac{1}{\gamma^2} + \theta^2 + \varphi_j^2 \right) t + \frac{c^2 t^3}{3\rho^2} + \frac{ct^2}{\rho} \varphi_j \right] \right) dt. \quad (\text{D4})$$

Since the radiation is beamed in a narrow cone that sweeps cross the observation point, we are only interested in the case with $\theta = 0$. Thus

$$\begin{aligned} A_{\parallel,j} &\simeq \int_{-\infty}^{\infty} \left(\frac{ct}{\rho} + \varphi_j \right) \exp \left(i \frac{\omega}{2} \left[\left(\frac{1}{\gamma^2} + \varphi_j^2 \right) t + \frac{c^2 t^3}{3\rho^2} + \frac{ct^2}{\rho} \varphi_j \right] \right) dt, \\ A_{\perp,j} &\simeq 0. \end{aligned} \quad (\text{D5})$$

Let us define

$$x = \frac{ct}{\rho} \left(\frac{1}{\gamma^2} + \varphi_j^2 \right)^{-1/2}, \quad (\text{D6})$$

$$\xi = \frac{\omega\rho}{3c} \left(\frac{1}{\gamma^2} + \varphi_j^2 \right)^{3/2}, \quad (\text{D7})$$

one then has

$$A_{\parallel,j} \simeq \frac{\rho}{c} \left(\frac{1}{\gamma^2} + \varphi_j^2 \right) \int_{-\infty}^{\infty} \left(x + \frac{\varphi_j}{\sqrt{1/\gamma^2 + \varphi_j^2}} \right) \exp \left(i \frac{3}{2} \xi \left(x + \frac{1}{3} x^3 + \frac{\varphi_j}{\sqrt{1/\gamma^2 + \varphi_j^2}} x^2 \right) \right) dx. \quad (\text{D8})$$

Note that $x + x^3/3 + (\varphi_j/\sqrt{1/\gamma^2 + \varphi_j^2})x^2 \rightarrow x$ for $x \rightarrow 0$ and $x + x^3/3 + (\varphi_j/\sqrt{1/\gamma^2 + \varphi_j^2})x^2 \rightarrow x^3/3$ for $x \rightarrow \pm\infty$. Therefore, the following approximations are reasonable, e.g.

$$\begin{aligned} \int_{-\infty}^{\infty} x \exp \left(i \frac{3}{2} \xi \left(x + \frac{1}{3} x^3 + \frac{\varphi_j}{\sqrt{1/\gamma^2 + \varphi_j^2}} x^2 \right) \right) &\simeq \int_{-\infty}^{\infty} x \exp \left(i \frac{3}{2} \xi \left(x + \frac{1}{3} x^3 \right) \right) = \frac{2i}{\sqrt{3}} K_{2/3}(\xi), \\ \int_{-\infty}^{\infty} \exp \left(i \frac{3}{2} \xi \left(x + \frac{1}{3} x^3 + \frac{\varphi_j}{\sqrt{1/\gamma^2 + \varphi_j^2}} x^2 \right) \right) &\simeq \int_{-\infty}^{\infty} \exp \left(i \frac{3}{2} \xi \left(x + \frac{1}{3} x^3 \right) \right) = \frac{2}{\sqrt{3}} K_{1/3}(\xi). \end{aligned} \quad (\text{D9})$$

Finally, one has

$$\begin{aligned} A_{\parallel,j} &\simeq \frac{2i}{\sqrt{3}} \frac{\rho}{c} \left(\frac{1}{\gamma^2} + \varphi_j^2 \right) K_{2/3}(\xi) + \frac{2}{\sqrt{3}} \frac{\rho}{c} \varphi_j \left(\frac{1}{\gamma^2} + \varphi_j^2 \right)^{1/2} K_{1/3}(\xi), \\ A_{\perp,j} &\simeq 0. \end{aligned} \quad (\text{D10})$$

We assume that the bunch opening angle of the N trajectories is 2φ , and each trajectory is uniformly spaced in the

bunch opening angle. In this case, the second term in $A_{\parallel,j}$ will be zero. Thus, one has

$$\begin{aligned} \sum_j^N A_{\parallel,j}(\omega) &= \frac{N}{2\varphi} \int_{-\varphi}^{\varphi} \frac{\rho}{c} \left(\frac{1}{\gamma^2} + \varphi'^2 \right) \frac{2i}{\sqrt{3}} K_{2/3}(\xi) d\varphi' \\ \sum_j^N A_{\perp,j}(\omega) &= 0. \end{aligned} \quad (\text{D11})$$

This result is as same as Eq.(C4), and the next calculation about the radiation will be as same as Appendix C. We consider that the energy distribution of the electrons satisfies the power-law distribution, e.g. $N_e(\gamma)d\gamma = N_{e,0}(\gamma/\gamma_1)^{-p}d\gamma$ for $\gamma_1 < \gamma < \gamma_2$. If $\omega_\varphi \ll \omega_{c1}$, the energy radiated per unit frequency interval per unit solid angle is given by

$$\frac{dI}{d\omega d\Omega} = \frac{e^2}{c} \frac{2^{(2p-6)/3}}{3\pi^2} \left[\Gamma\left(\frac{2}{3}\right) \Gamma\left(\frac{p-1}{3}\right) \right]^2 N_{e,0}^2 \gamma_1^4 \begin{cases} \left(\frac{\omega}{\omega_{c1}}\right)^{2/3}, & \omega \ll \omega_\varphi, \\ \left(\frac{\omega_\varphi}{\omega_{c1}}\right)^{2/3}, & \omega_\varphi \ll \omega \ll \omega_{c1}, \\ \left(\frac{\omega_\varphi}{\omega_{c1}}\right)^{2/3} \left(\frac{\omega}{\omega_{c1}}\right)^{-(2p-2)/3}, & \omega \gg \omega_{c1} \end{cases} \quad (\text{D12})$$

If $\omega_\varphi \ll \omega_c$, the energy radiated per unit frequency interval per unit solid angle is given by

$$\frac{dI}{d\omega d\Omega} = \frac{e^2}{c} \frac{2^{(2p-6)/3}}{3\pi^2} \left[\Gamma\left(\frac{2}{3}\right) \Gamma\left(\frac{p-1}{3}\right) \right]^2 N_{e,0}^2 \gamma_1^4 \begin{cases} \left(\frac{\omega}{\omega_{c1}}\right)^{2/3}, & \omega \ll \omega_{c1}, \\ \left(\frac{\omega}{\omega_{c1}}\right)^{-(2p-4)/3}, & \omega_{c1} \ll \omega \ll \omega_\varphi, \\ \left(\frac{\omega_\varphi}{\omega_{c1}}\right)^{-(2p-4)/3} \left(\frac{\omega}{\omega_\varphi}\right)^{-(2p-2)/3}, & \omega \gg \omega_\varphi. \end{cases} \quad (\text{D13})$$

E. DIPOLE MAGNETOSPHERE GEOMETRY

In this section, we make a brief summary about the dipole magnetosphere geometry. For a magnetic dipole field, the field line in the polar coordinates (r, θ) is given by

$$r = R_{\max} \sin^2 \theta, \quad (\text{E1})$$

where R_{\max} denotes the distance at which the field line crosses the equator. For a field line with a certain R_{\max} , the curvature radius at (r, θ) is given

$$\begin{aligned} \rho &= \frac{(r^2 + r'^2)^{3/2}}{|r^2 + 2r'r'' - rr''|} = \frac{1}{3} R_{\max} \sin^4 \theta \frac{(1 + 4 \cot^2 \theta)^{3/2}}{1 + \cos^2 \theta} \\ &= \frac{1}{3} R_{\max} (1 - \mu^2)^{1/2} \frac{(1 + 3\mu^2)^{3/2}}{1 + \mu^2} \\ \rho &\simeq \frac{4}{3} R_{\max} \sin \theta \simeq \frac{4r}{3 \sin \theta} \quad \text{for } \theta \lesssim 0.5, \end{aligned} \quad (\text{E2})$$

where r' and r'' denote the first and second derivatives to θ , and μ is defined as $\mu = \cos \theta$. According to Eq.(E1), the differential length of the dipole field line is given by

$$dl = -R_{\max} \sqrt{1 + 3 \cos^2 \theta} d(\cos \theta). \quad (\text{E3})$$

Therefore, the total length from the origin to a point (r, θ) is given by

$$\begin{aligned} l &= R_{\max} \left[1 + \frac{\ln(2 + \sqrt{3})}{2\sqrt{3}} - \left(\frac{1}{2} \mu \sqrt{1 + 3\mu^2} + \frac{\text{arcsinh}(\sqrt{3}\mu)}{2\sqrt{3}} \right) \right] \\ &\simeq R_{\max} (1 - \cos \theta) = r \frac{1 - \cos \theta}{\sin^2 \theta} \quad \text{for } \theta \lesssim 1. \end{aligned} \quad (\text{E4})$$

According Eq.(E2) and Eq.(E4), for a given length, the curvature radius satisfies

$$\begin{aligned} \frac{\rho}{l} &= \frac{1}{3}(1 - \mu^2)^{1/2} \frac{(1 + 3\mu^2)^{3/2}}{1 + \mu^2} \left[1 + \frac{\ln(2 + \sqrt{3})}{2\sqrt{3}} - \left(\frac{1}{2}\mu\sqrt{1 + 3\mu^2} + \frac{\operatorname{arcsinh}(\sqrt{3}\mu)}{2\sqrt{3}} \right) \right]^{-1} \\ &\simeq \frac{4}{3} \frac{\sin \theta}{1 - \cos \theta} \quad \text{for } \theta \ll 1. \end{aligned} \quad (\text{E5})$$

Note that: 1. the above formula is independent of R_{\max} , which means that it is applicable for all dipole field lines; 2. Due to $\delta\rho/\rho \sim \delta\theta/\sin\theta$, the curvature radius does not significantly changes for $\delta\theta \lesssim 0.1\theta$. Next, we define β as the angle between the radial direction and the magnetic field, which is given by

$$\cos \beta = \frac{2 \cos \theta}{\sqrt{1 + 3 \cos^2 \theta}}. \quad (\text{E6})$$

The difference of β satisfies

$$\frac{d\beta}{d\theta} = \frac{2}{1 + 3 \cos^2 \theta} \simeq \frac{1}{2} \quad \text{for } \theta \ll 1. \quad (\text{E7})$$

Then the angle between the magnetic axis and the magnetic field is $\alpha = \theta + \beta$, e.g.,

$$\alpha = \theta + \arccos \left(\frac{2 \cos \theta}{\sqrt{1 + 3 \cos^2 \theta}} \right), \quad (\text{E8})$$

and its corresponding difference reads

$$\frac{d\alpha}{d\theta} = \frac{3(1 + \cos^2 \theta)}{1 + 3 \cos^2 \theta} \simeq \frac{3}{2} \quad \text{for } \theta \ll 1. \quad (\text{E9})$$